

Study of LaBr₃ (Ce) Detector Response to High Energy Helium Ions

By

Christian Nayve

A Thesis Submitted in Partial Fulfillment

Of the Requirements for the Degree of

Master of Applied Science

In

Faculty of Energy Systems and Nuclear Science

Ontario Tech University

April 2022

©Christian Nayve, 2022

THESIS EXAMINATION INFORMATIONSubmitted by: **Christian Nayve****Master of Applied Science in Nuclear Engineering**

| |
|--|
| Thesis title: Study of LaBr ₃ (Ce) Detector Response to High Energy Helium Ions |
|--|

An oral defense of this thesis took place on April 11th,2022 in front of the following examining committee:

Examining Committee:

| | |
|------------------------------|-----------------------|
| Chair of Examining Committee | Dr. Jennifer McKellar |
| Research Supervisor | Dr. Rachid Machrafi |
| Examining Committee Member | Dr. Igor Pioro |
| Examining Committee Member | Dr. Kirk Atkinson |
| Thesis Examiner | Dr. Filippo Genco |

The above committee determined that the thesis is acceptable in form and content and that a satisfactory knowledge of the field covered by the thesis was demonstrated by the candidate during an oral examination. A signed copy of the Certificate of Approval is available from the School of Graduate and Postdoctoral Studies.

ABSTRACT

The space radiation environment is a complex mixed field composed of neutral and charged particles such as photons, protons, alpha, and other particles. The mixture of these different particles creates a challenge in any accurate measurement with radiation detection devices. Lanthanum Bromide scintillator detector ($\text{LaBr}_3: \text{Ce}$) has been successfully used as a gamma spectrometer inside space crafts. However, data on its response to other particles such as charged particles remains limited. From a radiation protection perspective, it is important to understand the response of the LaBr_3 scintillator in the presence of heavy ions to provide more accurate measurements of the gamma fields within such a complex radiation environment. A series of Monte-Carlo simulations using MCNP/X version 2.6 have been performed along with a series of experiments using the Heavy Ion Medical Accelerator in Chiba, Japan. Measurements of the detector response function were conducted using He ion beams at various energies.

Keywords:

Helium Ions; Lanthanum Bromide; Scintillator; Response; MCNP/X

AUTHOR'S DECLARATION

I hereby declare that this thesis consists of original work of which I have authored. This is a true copy of the thesis, including any required final revisions, as accepted by my examiners.

I authorize the University of Ontario Institute of Technology (Ontario Tech University) to lend this thesis to other institutions or individuals for the purpose of scholarly research. I further authorize University of Ontario Institute of Technology (Ontario Tech University) to reproduce this thesis by photocopying or by other means, in total or in part, at the request of other institutions or individuals for the purpose of scholarly research. I understand that my thesis will be made electronically available to the public.

Christian Nayve

YOUR NAME

STATEMENT OF CONTRIBUTIONS

The work that was done in Chapter 2 was done in the HIMAC facility in Chiba, Japan. The raw data and measurements are taken by Dr. Rachid Machrafi and Dr. Alex Miller using the Heavy Ion Accelerator. I was responsible for calibrating the detector, processing the raw measurements, and using the SRIM table to calculate the energy of the beam coming out of the BF. I also performed the simulations using MCNP/X version 2.6 and evaluated the response function curve of the detector.

ACKNOWLEDGEMENTS

I would like to thank Dr. Rachid Macrafi for providing the opportunity to work and learn under his supervision. His patience with me throughout my time here in these extraordinary circumstances was noticeable. Thank you to Dr. Alex Miller for taking the time to talk with me and answering all my questions about his work and this project.

I would like to thank NSERC for the support of this work. Furthermore, I would like to thank Dr. Eric Benton, Dr. Satoshi Kodaira, and the HIMAC facility staff for generously arranging and providing some beam time at the HIMAC facility for these experiments.

Finally, I want to thank all my friends and family for their unconditional support in my pursuit of a master's degree in these challenging times.

Table of Contents

| | |
|--|----------|
| THESIS EXAMINATION INFORMATION | i |
| ABSTRACT | ii |
| AUTHOR'S DECLARATION..... | iii |
| STATEMENT OF CONTRIBUTIONS..... | iv |
| ACKNOWLEDGEMENTS..... | v |
| LIST OF TABLES | ix |
| LIST OF FIGURES | x |
| LIST OF NOMENCLATURE..... | xii |
| Introduction | 1 |
| Chapter 1: Charged Particle Interaction and Detection | 6 |
| 1.1 Charge Particle Interaction with Matter | 7 |
| 2.1.2 Classification of Charge Particle | 8 |
| 2.1.2.1 Light charged particles..... | 8 |
| 1.1.1.2 Heavy Charged Particles | 8 |
| 1.1.2 Ionization | 9 |
| 1.1.2.1 Charge Particle Energy Per Ion Pair | 9 |
| 1.1.2.2 Specific Ionization | 9 |
| 1.1.3 Excitation | 10 |
| 1.1.4 Bremsstrahlung | 10 |
| 2.2 Energy Loss in Heavy Charged Particles | 12 |
| 1.2.1 Stopping Power and Linear Energy Transfer | 13 |
| 1.2.2 Bragg Curve..... | 16 |
| 2.3 Charge Particle Detection | 18 |
| 1.3.1 Types of Charged particle detectors..... | 18 |
| 1.3.1.1 Gas-Filled Detectors Detector | 18 |
| 1.3.1.1.1 Ionization Chamber..... | 19 |
| 1.3.1.1.2 Proportional Counters..... | 19 |

| | |
|--|-----------|
| 1.3.1.1.3 Geiger Muller Counters | 20 |
| 1.3.1.2 Scintillators | 21 |
| 1.3.1.2.1 Photomultiplier Tube | 23 |
| 1.3.1.2.2 Photodiodes | 24 |
| 1.3.1.3 Solid-state detectors | 24 |
| 1.3.2 Characteristics of Charge Particle Detectors | 25 |
| 1.3.2.1 Charge Particle Spectroscopy | 25 |
| 1.3.2.2 Energy Resolution | 27 |
| 1.3.1.3 Efficiency | 29 |
| 1.3.1.4 Light Output | 31 |
| 1.4 LaBr ₃ Crystal | 32 |
| 1.4.1 LaBr ₃ crystal compared to other scintillator materials | 32 |
| 1.4.2 LaBr ₃ crystal used in space missions | 35 |
| 1.4.2.1 Problems with crystal growth | 36 |
| 1.4.2.2 Energy Resolution and Crystal volume | 37 |
| 1.4.3 LaBr ₃ Detectors for Fission events | 38 |
| 1.4.4 Analytical expression for total and full energy peak efficiencies for LaBr ₃ : Ce Detectors | 39 |
| 1.4.4 LaBr ₃ Detectors in Portable Autonomous Radiation Detection | 42 |
| 1.4.5 LaBr ₃ Detector as an Environmental Radiation Monitor | 43 |
| Chapter 2: Methodology Description | 44 |
| 2.1. Modeling and Simulation | 44 |
| 2.1.1 MCNP Input file | 45 |
| 2.1.1.1 Cell block | 46 |
| 2.1.1.2 Surface Block | 46 |
| 3.1.2.1 Data Block | 48 |
| 3.1.3 Geometric Simulation Model of LaBr ₃ (Ce) Material | 50 |
| 2.1.2.1 MCNP/X Visual Editor | 50 |
| 2.2 Experimental Study | 55 |

| | |
|---|-----------|
| 2.2.1. Lanthanum Bromide Detector Characteristics | 55 |
| 2.2.1.1 Photomultiplier Tube | 58 |
| 2.2.1.2 Window material..... | 60 |
| 2.2.1.3 Photocathode Material | 61 |
| 2.2.1.4 Multichannel Analyzer..... | 62 |
| 2.2.2. Detector Calibration | 62 |
| 2.2.3. Experimental Setup and Facility | 65 |
| 2.2.4 Dose Depth Curve | 68 |
| Chapter 3: Results, Analysis, and Discussion | 69 |
| 3.1 Simulation Results..... | 69 |
| 3.2 Experimental Results..... | 69 |
| 3.3 Comparison Between Experimental Data and Simulation | 71 |
| 3.4 Deposited Energy Curve..... | 78 |
| 3.5 Response function | 80 |
| 3.6. Quenching effecting in He Ions | 83 |
| 3.7 Detector Characteristics..... | 84 |
| 3.7.1 Detector Resolution..... | 84 |
| 3.7.2 Error Analysis | 86 |
| Conclusions..... | 87 |
| Future Work..... | 89 |
| References..... | 90 |
| Appendix | 93 |
| Appendix A..... | 93 |
| Appendix B..... | 95 |
| Appendix C..... | 97 |
| Appendix D..... | 98 |
| Appendix E..... | 99 |

LIST OF TABLES

CHAPTER 1

| | |
|--|----|
| Table 1. 1 Comparison of LaBr ₃ and the most common scintillator detectors for 1 MeV gamma-rays [21]..... | 33 |
| Table 1. 2 Detector resolution with the increasing volume of the LaBr ₃ crystal [21] | 36 |
| Table 1. 3 Various LaBr ₃ detectors resolutions before and after proton irradiation [9] | 37 |

CHAPTER 2

| | |
|---|----|
| Table 2. 1 Different particles modes for base MNCP code [17] | 49 |
| Table 2. 2 Tally functions with the notations and a general description of the function [17]..... | 49 |
| Table 2. 3. Physical Characteristics of LaBr ₃ (Ce) [6]..... | 56 |
| Table 2. 4. Comparison of LaBr ₃ (Ce) properties with NaI (TI) [6] | 57 |
| Table 2. 5 Radionuclide sources used for the detector calibration [34]..... | 65 |

LIST OF FIGURES

CHAPTER 1

| | |
|--|----|
| Figure 1. 1 Electromagnetic spectrum | 7 |
| Figure 1. 2. The Bremsstrahlung interaction as an electron passes by the nucleus | 11 |
| Figure 1. 3. Bragg curve for heavy ions outlining the Bragg peak..... | 17 |
| Figure 1. 4. Outline of a gas-filled detector build [2] | 19 |
| Figure 1. 5. Voltage Regions of each Gas Detector [5] | 21 |
| Figure 1. 6. Energy structure of an activated crystal lattice [5]..... | 22 |
| Figure 1. 7. Ontario tech U solid-state detector..... | 25 |
| Figure 1. 8. Typical spectra for alpha particles. [2] | 26 |
| Figure 1. 9. Ideal energy deposition of a heavy charged particle in a detector | 27 |
| Figure 1. 10. Comparison between peaks with poor versus good resolution [5]..... | 28 |
| Figure 1. 11. Full energy peak for a spectrum [7] | 31 |
| Figure 1. 12. Schematic diagrams of the two PMT configurations | 35 |
| Figure 1. 13 Activation of the LaBr ₃ crystal with increasing proton flux [9]..... | 39 |
| Figure 1. 14 View of all the photon path lengths through the scintillator material cylinder from a point source [12] | 42 |

CHAPTER 2

| | |
|--|----|
| Figure 2. 1. Interaction using the gamma radiation to outline the possible outcomes through MCNP [15]..... | 45 |
| Figure 2. 2. 3-D view of LaBr ₃ crystal with the MCNP/X code | 52 |
| Figure 2. 3. SRIM table input window..... | 53 |
| Figure 2. 4. SRIM output table | 54 |
| Figure 2. 5. LaBr ₃ detector along with the photomultiplier tube attached to the MCA | 56 |
| Figure 2. 6 Image of the Hamamatsu R6231 PMT (left) and the diagram with the dynodes outlines (right) [33] | 59 |
| Figure 2. 7. Top-down view of the PMT..... | 59 |
| Figure 2. 8. Quantum efficiencies of different photocathode materials [33] | 60 |
| Figure 2. 9. Quantum Efficiency of varied materials in the PMT window [33] | 61 |

| | |
|--|----|
| Figure 2. 10. Calibration curve of the $\text{LaBr}_3(\text{Ce})$ detector | 64 |
| Figure 2. 11. 12-hour background count outlining the natural La peak..... | 64 |
| Figure 2. 12 Experimental Setup at HIMAC facility | 67 |
| Figure 2. 13. Diagram of the experimental setup | 67 |
| Figure 2. 14. Dose Depth Curve of the HIMAC He Ion Beam | 68 |

CHAPTER 3

| | |
|--|----|
| Figure 3. 1 Pulse Height Spectra of the MCNP/X simulation (top) and the experimental data (bottom) for 0mm and 20.24 mm BF | 70 |
| Figure 3. 2 Pulse Height Spectra of the MCNP/X simulation (top) and the experimental data (bottom) for 40.03mm and 60.32 mm BF | 72 |
| Figure 3. 3 Pulse Height Spectra of the MCNP/X simulation (top) and the experimental data (bottom) for 70.22mm and 90.05 mm BF | 73 |
| Figure 3. 4 Pulse Height Spectra of the MCNP/X simulation (top) and the experimental data (bottom) for 100.42mm and 120.18 mm BF | 75 |
| Figure 3. 5 Pulse Height Spectra of the MCNP/X simulation (top) and the experimental data (bottom) for 130.16 mm and 143.16 mm BF | 77 |
| Figure 3. 6 The peak energies in the crystal with respect to BF thickness for the MCNP/X data (top) and the peak channel for the experimental data (bottom)..... | 79 |
| Figure 3. 7. The experimental peak energy with respect to the simulation peak energy along with the gamma calibration. | 81 |
| Figure 3. 8. Full response curve of the crystal with the gamma peak and calibration with the He ion peak energies..... | 82 |
| Figure 3. 9 FWHM of the full peak at 10.41 mm BF | 84 |
| Figure 3. 10 FWHM of the full peak at 50.41 mm BF..... | 85 |
| Figure 3. 11 FWHM of the full peak at 140.22 mm BF..... | 86 |

LIST OF NOMENCLATURE

BGO: Bismuth Germanate

BF: Binary Filter (acrylic heavy charged particle beam blockers)

eV: Electron Volt

FWHM: Full Width at Half Maximum

keV: Kilo Electron Volt (1,000 eV)

MCA: Multichannel Analyzer

MCNP: Monte Carlo N-Particle Transport

MeV: Mega Electron Volt (1,000,000 eV)

NaI: Sodium Iodide

NIRS: National Institute of Radiological Sciences

GeV: Giga Electron Volt (1,000,000,000 eV)

Gy: Grey, absorbed dose (unit of J/kg)

HIMAC: Heavy Ion Medical Accelerator in Chiba

LaBr₃: Lanthanum Bromide

LaCl₃: Lanthanum Chloride

LET: Linear Energy Transfer

PMMA: Polymethylmethacrylate, acrylic

PMT: Photomultiplier Tube

SRIM: Stopping and Ranges of Ions in Matter (radiation simulation software)

ZnS: Zinc Sulfide

Introduction

Radiation is a recent discovery in the history of physics. The discovery of radiation can be traced back to Wilhelm Roentgen. It was first observed when he noticed the cathode ray tube continuing to glow after being covered by black cardboard, marking the first observation of x-rays and their detection of them. From there he realized that x-rays could release electrical charges from the air.

Continuing from this Roentgen continued to work with x-rays, using them as a means of imaging. In December 1885, he created the first medical image of his wife's hand using x-rays and photographic plates [1].

Henri Becquerel studied the effects of visible light in place of x-rays with phosphorescent plates on the photographer's plates by observing fluorescent uranium compounds over the plates, resulting in black spots on the plate. He continued using different fluorescent materials in the dark and concluded that x-ray-like radiation was being emitted from these uranium compounds. This was known later to be gamma radiation.

Continuing from Becquerel's work, Marie Curie continued working with uranium. She observed the proportional relationship between the radiation intensity and the amount of uranium. Along with her husband, Pierre Curie, they went on to discover polonium and radium as radiation emitters in 1898 which marked the beginning of a period of discovery in radiation emission.

The idea of radiation as waves and particles started to develop from Curie's work which encouraged further study into ionized materials. This field of study resulted in major discoveries

such as the biological damage caused by ionizing radiation. Different methods of detecting radiation started to develop like fluorescence screens, photographic plates, and ionization chambers. These methods were limited to the detection of high activity sources and could not measure low activities [1].

Photographic plates were developed extensively, and have been used in x-ray radiography, and studying cosmic rays. Gas-filled detectors were developed for alpha particle detection. A counter for beta detection was developed in 1913. These developments were the precursor for the famous Geiger Muller (GM) detector created by Geiger and Muller in 1928. The GM counter could detect diverse types of radiation, but the limitation was that it could not measure radiation or make any distinction on the levels of activity. In the 1940s, the proportional counter, a gas-filled detector, was introduced. This was used for x-ray spectroscopy at lower energies.

Scintillating light was studied in the 1930s for radiation detection. This was first explored using zinc sulfide (ZnS). However, it was not until the 1940s with the advent of the electronic photomultiplier that scintillator detectors were dependable. Inorganic scintillator materials like Sodium Iodide (NaI) became popular. The NaI scintillator became commercially available in the 1950s and are still being used today as gamma spectrometers and in medical imaging.

Semiconductor detectors were first introduced in the early 1960s. Semiconductor detectors are used for a wide range of radiation, depending on the material. Silicon, for instance, was used for low energy x-ray spectrometers; high purity germanium detectors are excellent for gamma detection and measurement.

The next step for radiation detection was the development of thermoluminescent dosimeters (TLD). These types of crystals can trap the energy deposited by the radiation. This energy could be released when exposed to higher temperatures. TLD is commonplace in radiation dosimetry.

The development and advancement of radiation detection and measurement were due in part to the advancement of electronics in these devices. Furthermore, the technology and software advancements in signal processing were key in radiation spectroscopy.

The type of detector used is dependent on two key factors. The first is the radiation that is being detected and the second is the energy range of the radiation. Thus, the wide variety of detectors can cover a variety of uses such as personal dosimeters, radiation monitors, or spectrometers.

The advent of radiation research led to the advancement of many different fields: the understanding and use of nuclear energy from power plants, the uses of radiation in medical imaging, medical treatment with radiation therapy to treat various kinds of cancers, and radiation as a means for sterilizing foods. The uses of radiation have become widespread in many different fields and industries. As such, the need for regulation and international standards for the handling and use of radiation increases [1,2].

Gamma rays are high-energy ionizing radiation that can lead to immediate biological damage with high enough doses. Furthermore, gamma radiation can damage sensitive electronics. Therefore, its detection is crucial to prevent harm to humans and electronic failure leading to higher costs. There is a wide range of scintillators that can be used for gamma detectors. NaI scintillators have been the choice of gamma detectors due to their decent resolution for spectroscopy.

The scintillation techniques have led to the utilization of the pulse height spectrum produced by these detectors. An increasing number of counts at the peaks, resolution, and accuracy have resulted in the development of higher performance isotope identification systems using the NaI (TI) scintillator. Lanthanum halide detectors are new scintillator crystals and have become more commonplace in gamma spectroscopy in a wide variety of fields. They are popular due to their good resolution, greater light output, and better timing detector properties compared to other scintillator materials. These new scintillator materials are significantly more expensive and cannot be produced in large volumes. However, the LaBr₃ crystal has shown improved quality of gamma detection.

The LaBr₃ crystal has become widely used in various areas due to its superior scintillating properties stated previously. It has been recently integrated into space missions as a gamma-ray spectrometer. However, space is a mixed field of radiation, composed of gamma rays, protons, alpha particles, neutrons, and various other forms of radiation. The response of the LaBr₃ crystal to these and other forms of radiation has not been well characterized. From a radiation protection perspective, it is important to understand the response of the LaBr₃ scintillator in the presence of heavy ions to provide more accurate measurements of the gamma field.

The focus of this study is to explore and understand the response of the Lanthanum Bromide (LaBr₃: Ce) detector in presence of high-energy He ions as a part of its response to complex radiation fields. More specifically:

1. Expose LaBr₃ scintillator crystal to high energy He ions at different energies and measure the pulse height spectrum at different energies.

2. Simulate the experimental conditions using Monte Carlo simulations MCNP/X code and SRIM calculations in Chapter 2.
3. Investigate the response of the detector to high-energy He ions by comparing the pulse height spectra of both experimental and simulated conditions.
4. Analyzing the detector response to high energy He ion and gamma radiation to extract the light output of the scintillator.

This thesis consists of an introduction, three chapters, a conclusion, and future work. The thesis ends with a list of references and appendices. The introduction gives a brief historic overview of radiation, and radiation detection and measurement. Chapter one is dedicated to charged particle interactions with a focus on heavy charged particle interaction with matter and the LaBr_3 crystal. Chapter two describes the methodology of this work, which includes the experimental setup at the HIMAC facility in Chiba, Japan. The SRIM tables are used to calculate the energy of the beams. Furthermore, this chapter includes Monte Carlo code using MCNP/X version 2.6 to simulate the experimental setup for the detector response function. A description of the LaBr_3 scintillator with the photomultiplier tubes used, multichannel analyzer, and the data acquisition system used in the setup are also discussed in chapter two. Chapter three contains the results of the MCNP/X modeling, the experimental results, and the response function of the scintillator. The conclusion summarizes the key points of the study and provides some future work that may benefit radiation measurement in space.

Chapter 1: Charged Particle Interaction and Detection

Electromagnetic radiation is defined as the transmission of particles or waves without the need for a medium present (in a vacuum). There are two classifications of radiation: a) ionizing radiation (charged particles, neutrons, gamma, x-rays) and b) nonionizing radiation (visible light, microwaves, radio waves). Figure 1 outlines the distinctions of electromagnetic radiation by energy and wavelength. Ionizing radiation is electromagnetic radiation with sufficient energy to liberate an electron from atoms, thus creating ions.

Ionizing radiation is further divided into charged particles composed of a positive (proton, alpha particles) charge, negative (beta particles) charge, or particles that have a neutral charge like a neutron. Charged particles are classified into light and heavy charged particles [4,6].

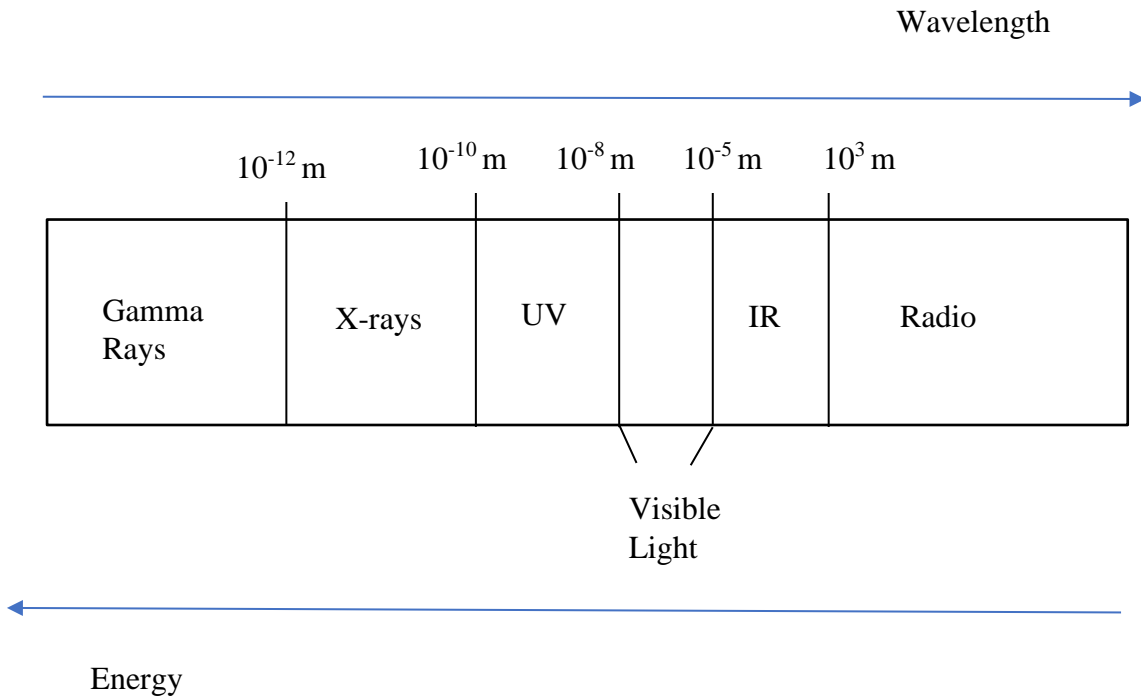


Figure 1. 1 Electromagnetic spectrum

1.1 Charge Particle Interaction with Matter

Charged particles are further classified into two categories: light charged particles and heavy charged particles. The interactions the particles have with the medium change with the size and the charge of the particle. Particles travelling through a medium deposit their energy into that medium.

2.1.2 Classification of Charge Particle

2.1.2.1 Light charged particles

There are many types of light charged particles, but the two main particles are electrons and positrons. Light charged particles lose energy through two different mechanisms: collisional and radiative losses.

1.1.1.2 Heavy Charged Particles

Heavy charged particles are defined by particles with atomic masses $A \geq 1$. Protons and alpha particles follow these criteria. Heavy charged particles have distinct interactions with matter that differ from light charged particles

First, are the differences in masses. A proton is 2000 times greater in mass compared to an electron and an alpha is 7000 times greater in mass than that of an electron. These heavier particles experience greater Coulomb forces – especially the alpha since it has a greater charge.

Heavy charged particles lose energy primarily through ionization and excitation of the surrounding atoms in the medium. Due to the masses of these particles, heavy charged particles only lose a small fraction of their kinetic energy in a single interaction. Unlike light charged particles, deflections in collisions are insignificant. Therefore, heavy charged particles always travel in a linear path through matter. It continuously loses energy mostly through numerous collisions with atomic electrons in the medium [4].

1.1.2 Ionization

Charged particles can remove one or multiple electrons from an atom or molecule because of the Coulomb forces that are being exerted onto the outermost electrons, attracting, or repelling the electron depending on the charge of the particle. For the electron to be liberated from the atom, the charged particle must transfer sufficient energy to match or exceed the electron's binding energy to the atom.

When an atom is ionized, an ion pair is formed where the atom or molecule ion becomes positively charged by the release of an electron. The electron is released with some kinetic energy depending on the energy that has been imparted. This additional energy can also ionize other atoms. This secondary ionization from the secondary electron is called delta rays [4].

1.1.2.1 Charge Particle Energy Per Ion Pair

The energy lost by the charged particle when it produces an ion pair is known as the "W" value. This depends on the type of charged particle and the material that the particle is travelling through. The "W" values do not change with different particle energies but, with heavier charged particles the W value increases at low energies. For example, beta particles lose on average 34 eV per ion pair produced in the air and alpha particles lose 36 eV per ion pair produced in air. From these values, the W value does not differ significantly.

1.1.2.2 Specific Ionization

Specific ionization refers to the average number of ion pairs that are produced per unit distance travelled by the incident charged particle through the medium. Several factors determine the

specific ionization for different charged particles. First is the type of charged particle. Heavier particles interact more with the medium and create more ion pairs. Another is energy, a particle can create more ion pairs with increasing energy. Finally, the material the particle is travelling through also influences the specific ionization. Materials that are denser or have large Z values contain more electrons for the particle to interact with [4]. For reference, alpha particles create between 20000-60000 ion pairs per centimetre and beta particles create around 100 ion pairs per cm.

1.1.3 Excitation

If the charged particle does not provide sufficient energy to cause ionization, the electrons in the atom undergo excitation. The electrons in the atom are forced into a higher energy level and then goes back into its ground configuration. The transition from the excited to ground state of the electron releases a photon. This photon energy is in the visible light wavelength range or even higher in ultraviolet range. It is important to note that excitation occurs more frequently farther along the particle's path [4].

1.1.4 Bremsstrahlung

Bremsstrahlung radiation occurs when a charged particle undergoes deceleration. This deceleration causes the charged particle to emit a photon. This change in acceleration is caused by an electron travelling close to the nucleus. The positive charge of the nucleus causes the acceleration. This case can only apply to light charge particles since they are small enough to cause the deflection needed to create the photon. If the particle carries sufficient kinetic energy, it emits this special case of radiation. For light charged particles like electrons, bremsstrahlung photons

have a continuous energy distribution. The maximum energy of this photon equals the kinetic energy of the oncoming electron [4].

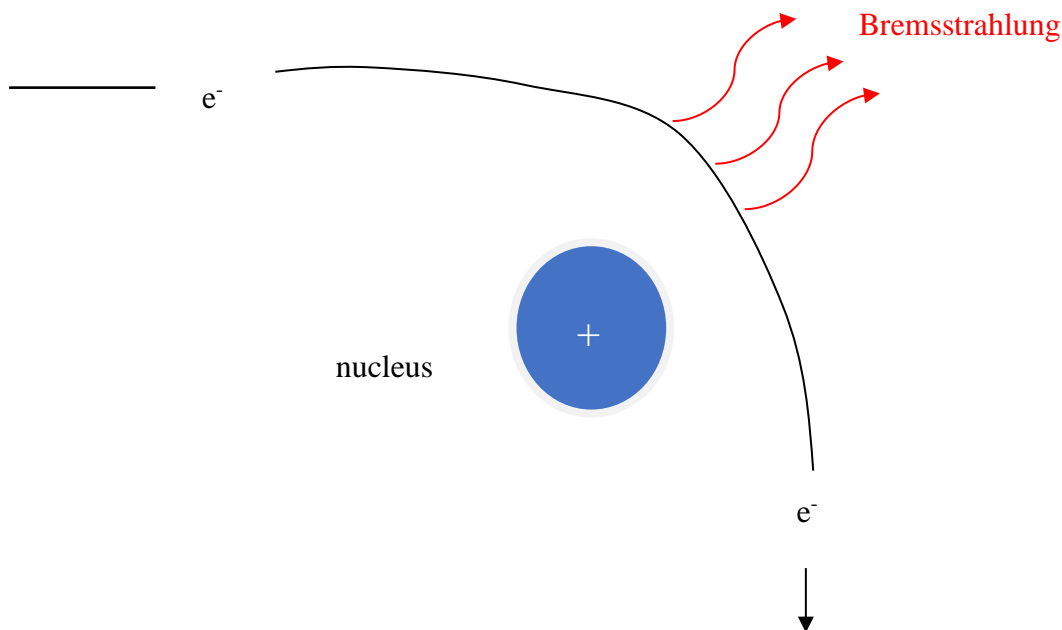


Figure 1. 2. The Bremsstrahlung interaction as an electron passes by the nucleus

It is important to note that Bremsstrahlung radiation does not coincide with nuclear or electronic transitions. However, the photon that this emits could excite another electron and or nucleus. This leads to the emission of other radiation such as gamma rays (nuclear transitions) or x-rays (electronic transitions). The efficiency of the Bremsstrahlung is dependent on the Z^2 of the medium. This means that for any energy of beta particles, mediums with high Z results greater energy losses

due to bremsstrahlung interaction being more significant. Bremsstrahlung photons energy increases with a greater kinetic energy of the light charged particles.

Radiation yield can be defined as the average fraction of its energy the beta particle yields as bremsstrahlung when it slows down completely. This can be estimated using this relationship:

$$Y = \frac{6 * 10^{-4} ZT}{1 + 6 * 10^{-4} ZT} \quad (1)$$

- Y is the radiative yield of the particles
- T is the kinetic energy of the particle in MeV
- Z is the atomic number of the medium the particles is travelling through

2.2 Energy Loss in Heavy Charged Particles

For heavy charged particles, the maximum energy transfer through a single interaction can be determined by looking at the conservation of energy and momentum.

$$\frac{1}{2} MV^2 = \frac{1}{2} MV_1^2 + \frac{1}{2} mv_1^2 \quad (2)$$

$$MV = MV_1 + mv \quad (3)$$

- M and m are the masses of the heavy charged particle and the electrons respectively in kg.
- V₁ and v₁ are the velocities of the heavy charged particle and the electron after the collision respectively, in m/s.

Using both these relationships, the maximum energy transfer can be determined by:

$$Q_{max} = \frac{1}{2}MV^2 - \frac{1}{2}MV_1^2 = \frac{4mME}{(M + m)^2} \quad (4)$$

Considering relativistic effects (particles speeds that are comparable to fractions of the speed of light), the maximum energy transfer of a single collision for heavy charged particles can be generalized using the following:

$$Q_{max} = \frac{2\gamma^2 mV^2}{1 + 2\gamma \left(\frac{m}{M}\right) + \left(\frac{m^2}{M^2}\right)} \quad (5)$$

Where:

- γ is the Lorenz factor.
- $\beta = V/c$

1.2.1 Stopping Power and Linear Energy Transfer

The stopping power for charged particles describes the total energy lost by the particle as it travels through the medium. Linear energy transfer (LET) refers to the energy that is lost by the charged particle and then locally absorbed by the medium the particle is traveling through. LET is referred to as the restricted stopping power, inferring those secondary electrons produced by these interactions do not travel past the volume of interest, and the energy is deposited locally [4].

The linear stopping power of heavy charged particles can be described using the semi-classical Bethe formula:

$$-\left(\frac{dE}{dx}\right) = \frac{4\pi k_0^2 z^2 e^4 n}{mc^2 \beta^2} \left[\ln \frac{2mc^2 \beta^2}{I(1-\beta^2)} - \beta^2 \right] \quad (6)$$

$$\frac{dE}{dx} = \frac{4\pi k_0^2 z^2 e^4 n}{mv^2} \ln \ln \left(\frac{mV^2}{hf} \right) \quad (7)$$

- $k_0 = 8.99 \times 10^9 \text{ N m}^2 \text{ C}^{-2}$
- z = atomic number of the heavy charged particles
- e = the electron charge
- n = electron density per unit volume of the medium
- m = rest mass of the electron, kg
- c = speed of light in a vacuum
- $B = V/c$
- I = mean excitation energy of the medium

The mean excitation energy (I) of a medium is related to the Z of the medium and thus can be approximated by the following relationships:

- $I=19.0 \text{ eV}$ if $Z=1$
- $I=11.2+11.7*Z \text{ eV}$, $2 \leq Z \leq 13$
- $I=52+8.71*Z \text{ eV}$, $Z>13$

The Bethe formula can be even further simplified for heavy charged particles:

$$-\left(\frac{dE}{dx}\right) = \frac{5.08 * 10^{-31} z^2 n}{\beta^2} \left[\ln \frac{1.02 * 10^6 \beta^2}{I(1-\beta^2)} - \beta^2 \right] \text{MeVcm}^{-1} \quad (8)$$

Describing the interactions of heavy charged particles penetrating matter analytically relies on the accuracy of the modified Bethe formula. However, there are limitations. The Bethe formula is only valid at high energies. At low energies, this approximation fails because at some point the log term becomes negative. The Bethe formula does not account for other interactions at low energies like electron capturing, which reduces the charge of the particle thus reducing the overall stopping power [4].

LET, or restricted stopping power, is introduced to better describe the energy lost in a target rather than the energy that is absorbed. For heavy charge particles, it travels within a linear path creating a notable number of secondary electrons or delta rays. These delta rays can hold a significant amount of energy. It is necessary, then, to separate the delta ray energy from the energy deposited locally by the heavy charged particle. LET is useful when understanding the energy deposition of the incident particle in local regions that have finite size overall. The delta rays' range needs to be considered, especially when the range is larger compared to the region of interest.

LET can be defined as the fraction of the mass collision stopping power that includes all soft collisions and hard collisions that result in delta rays with energy less than Δ .

$$LET_{\Delta} = \left(-\frac{dE}{dx} \right)_{\Delta} \quad (9)$$

Understanding the range of ionizing radiation is important for radiation detection and protection as it allows us to understand how different forms of radiation penetrate a given medium. For heavy

charge particles specifically, the range is related to the stopping power of the particles and can be determined using the relationship:

$$R(T) = \int_0^T \left(-\frac{dE}{dx} \right)^{-1} dE \quad (10)$$

From the relationship above, the range of a heavy charged particle can be determined if the range of another heavy charge particle is known with the same speed.

$$\frac{R_1(\beta)}{R_2(\beta)} = \frac{z_2^2 M_1}{z_1^2 M_2} \quad (11)$$

And using a proton as the reference the relationship becomes:

$$R(\beta) = \frac{M}{z^2} R_{proton}(\beta) \quad (12)$$

These ranges of protons have been measured and tabulated for air and water [4].

For charged particles, statistical fluctuations occur as the particles penetrate matter for the number of collisions along the path and the energy deposition for each interaction. Identical particles with the same conditions undergo different paths, and it is important to show a distribution of energies through a given depth and a distribution of path length.

1.2.2 Bragg Curve

The Bragg curve visually describes the interactions of charged particles as it travels through matter.

The Bragg curve plots the stopping power of the particles with respect to the depth or the path length of the particle.

The Bragg curve differs for several types of ionizing radiation and is useful when looking at the energy deposition of heavy charged particles. Figure 1.3 presents the typical shape of the Bragg curve of heavy charged particles. For most of the path length, the stopping power does not change much and is small. At higher energies, particles do not interact much with the medium and thus the energy transfer is low. The key property of heavy charged particles that is the particle deposits most of its energy at the end of the path length of the particle. This energy deposition by the heavy charged particle is called the Bragg peak and is seen in figure 1.3 [4,7].

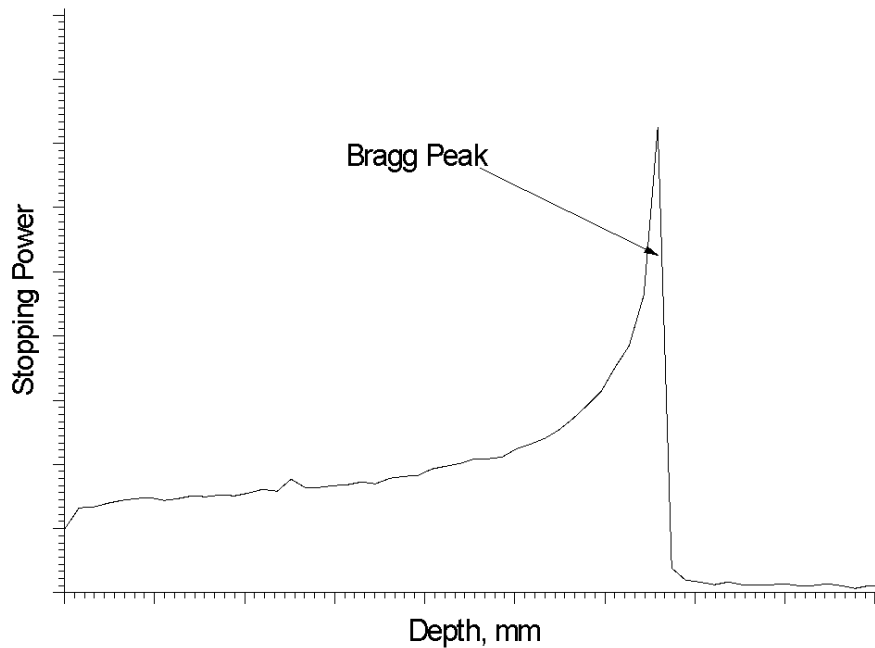


Figure 1. 3. Bragg curve for heavy ions outlining the Bragg peak

2.3 Charge Particle Detection

Charged particles deposit their energy into the medium by either ionizing the atoms around or forcing the electrons to undergo excitation. Thus, charged particle detection must rely on these interactions to measure this type of ionizing radiation. The sections below describe distinct types of detectors used for charged particle detection and measurements.

1.3.1 Types of Charged particle detectors

Two main types of detectors are used for charged particle detection. Gas-filled detectors and scintillation detectors. Each type can be further broken down into more specific categories which are described in the upcoming sections.

1.3.1.1 Gas-Filled Detectors Detector

The gas-filled detector has two main components that are key for radiation detection. The first is the cylindrical chamber walls (cathode) where the chamber contains pressurized gas. Next is a thin wire inside the chamber (anode). Gas-filled chambers rely on the ionization of the gas and an applied potential difference in the chamber. The potential difference in the chamber between the cathode and anode accelerates these electrons into the anode. A basic diagram of a gas-filled detector is described in this figure 1.4.

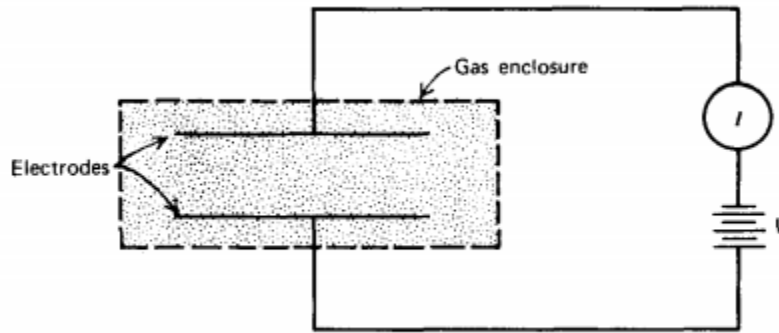


Figure 1. 4. Outline of a gas-filled detector build [2]

Gas-filled detectors have distinct functions depending on the operating voltage that is applied between the electrodes. The several types of gas detectors and their voltage region are outlined in figure 1.5.

1.3.1.1.1 Ionization Chamber

Ionization chambers have low applied voltages and only the primary electrons that are produced by the initial interactions are collected. The signal output is proportional to the deposited energy of the charged particle [2,5].

1.3.1.1.2 Proportional Counters

When the operating voltage between the electrodes increases, the kinetic energy of the electrons being collected by the anode increases. This increase in kinetic energy causes the primary electrons to undergo collisions and produce secondary electrons. The signal output of the proportional

counter increases, but it is still proportional to the deposited energy of the initial charge particle. Proportional counters can be used for gamma spectroscopy, with intermediate energy resolution.

1.3.1.1.3 Geiger Muller Counters

The operating voltage is further increased with GM counters. When this happens, it accelerates the primary electrons to the point that the current pulse becomes independent from the initial energy of the incident particle. Radiation types and energies cannot be differentiated at this point. GM counters are purely for detecting the presence of any type of ionizing radiation.

Gas-filled detectors are cheap and easier to produce compared to other radiation detectors. However, gas-filled detectors have poor energy measurements because of the low Z and very low density of a gas. The potential for radiation to pass through the chamber is likewise higher. [2,5].

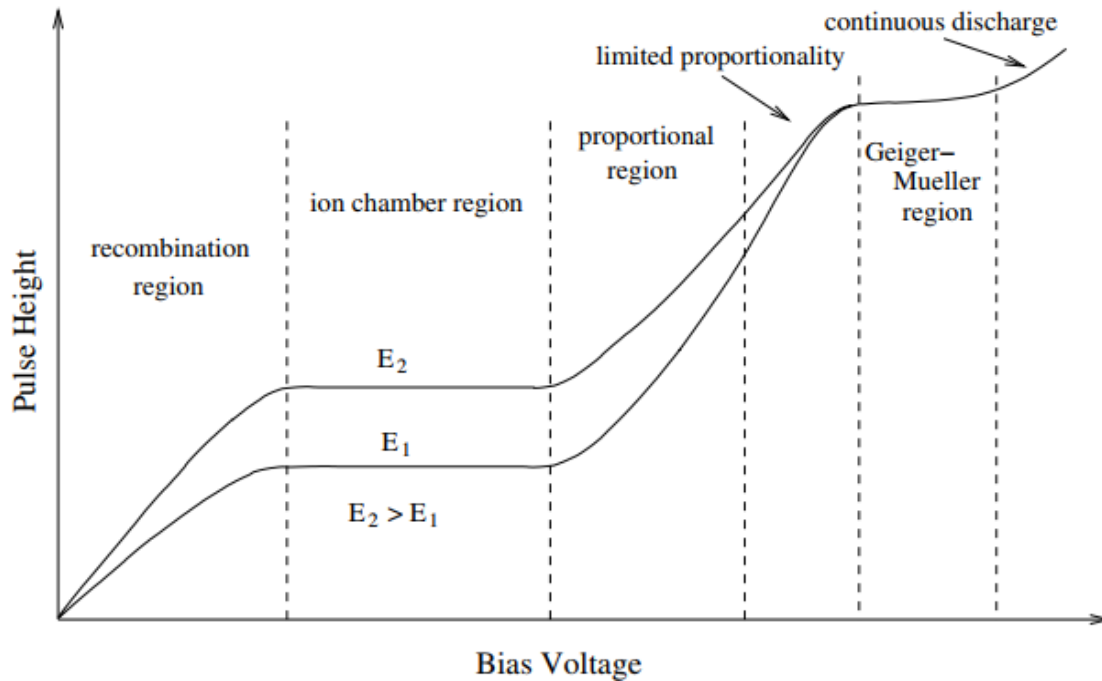


Figure 1. 5. Voltage Regions of each Gas Detector [5]

1.3.1.2 Scintillators

Scintillators are materials of any state that emits light when it undergoes excitation. The light output of the material is proportional to the energy that is deposited into the scintillator. This property of scintillators is a key mechanism for charged particle detection and measurement. Scintillators can be either organic or inorganic materials. Organic materials contain carbons and hydrogen chains. Inorganic scintillators are primarily characterized by their high density and Z crystalline structure (lattice); examples of scintillator crystals are NaI and CsI. In crystal lattice structures, electrons can only occupy selected energy bands. The gaps between these bands are energy values in which electrons are not found. This gap is known as the band gap or the forbidden gap. When energy is absorbed in a pure crystal (no impurities) the absorption of energy elevates

electrons from the valence band (ground) to what is known as the conduction band. This leaves a hole in the valence band. The electrons then return to the valence band emitting a photon. However, this process is inefficient in pure crystals, and the emission of a photon is few per decay of the electron, with the energy being released through other means.

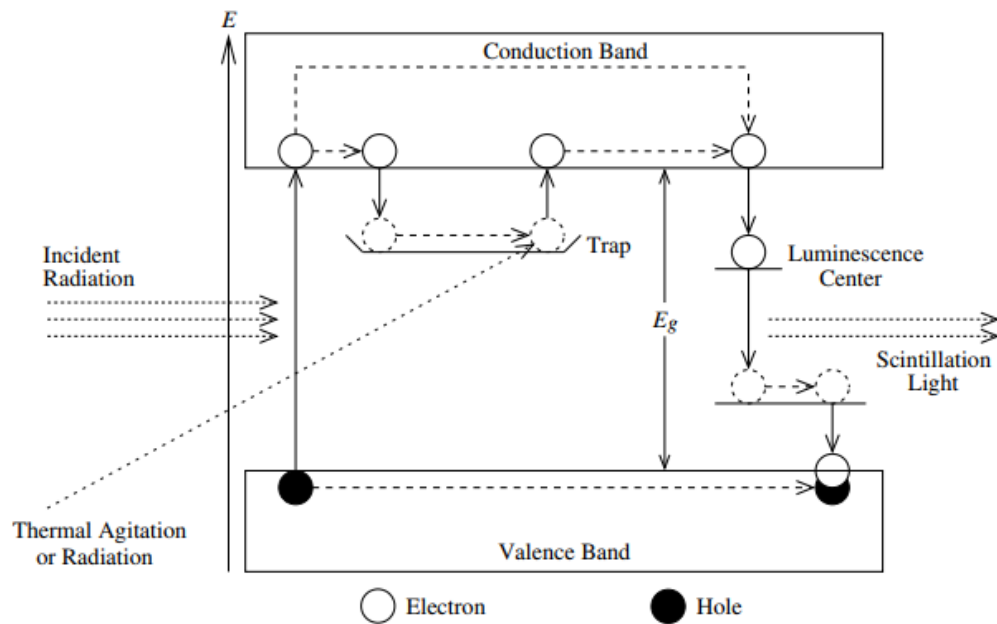


Figure 1. 6. Energy structure of an activated crystal lattice [5]

Furthermore, the distance of the band gap results in the photon being too high to be within the visible range with pure crystals. To address this, tiny amounts of impurities must be added to the crystal called activators. These activators modify the band gap of the crystal by creating energy states between the band gap where the electron reaches and de-excites back into the valence band. The energy states created by the activators have a small distance band which allows photons to be

emitted into the visible wavelength [7]. Figure 1.6 highlights the structure of the crystal with activators.

Organic materials operate differently compared to inorganic crystals. For organic structures, the emission of light is due to the transition of energy of a single molecule. Electrons can be placed in a variety of excited states or singlet states (s_1 , s_2 , s_3 , etc.). The transition between s_0 and s_1 is 3-4 eV and it becomes increasingly smaller. Each S level is subdivided into finer levels with 0.15 eV spacing. At room temperature, all electrons start at ground state s_0 . Electrons at s_2 and above drop to s_1 in a matter of picoseconds and this transition is radiation-less. Molecules in sub-states like $s_{1,1}$ or $s_{1,2}$ lose energy quickly because they are not in equilibrium with adjacent molecules. The emission of light is from the transition from $s_{1,0}$ to the ground state [7,8].

Regardless of the type of scintillator material used, the light produced from scintillation must be converted into an electrical signal. This is done with two different devices, the photomultiplier tube (PMT) or a photodiode.

1.3.1.2.1 Photomultiplier Tube

The first part of the PMT is the photocathode. When a photon interacts with the photocathode, it releases a low-energy electron in a vacuum. This is done through the process of the photoelectric effect in which an electron is released to the absorption of the photon energy in a photocathode.

With the release of the electron, the electrical signal from the photocathode is amplified through the process of electron multiplication. To do this, the PMT uses a series of dynodes where the electron goes through several stages of multiplication to produce 10^6 electrons. When the electron is ejected from the photocathode, it accelerates from a potential difference of hundreds of volts.

The kinetic energy gained from the electron creates secondary electrons by the dynode. These secondary electrons then accelerate to the second dynode and repeat the same process. This can be repeated several times before the electrons reach the anode to produce a stronger signal [2,7].

1.3.1.2.2 Photodiodes

Another method of converting scintillation light is using silicon photodiodes. This photodiode is a semiconductor device with a thin layer of silicon. The light is absorbed by the silicon which creates free charge carriers. These charge carriers consist of electrons and holes (a pseudo-particle that is created when the electron leaves) where the hole carries a positive charge. The electrons and holes are collected by the anode and cathode of the diode. The photodiode is new compared to the PMT, it is more compact than the PMT and has higher quantum efficiency. However, the photodiode struggles with electronic noise due to the small signal amplitude.

1.3.1.3 Solid-state detectors

Solid-state detectors or semiconductor detectors, compared to gas and scintillator detectors, are new. They operate similarly to inorganic scintillation where the electrons get excited in the solid-state crystal. These electrons move up to the conduction band and a current pulse is created.

A type of solid-state detector is a high purity Germanium (HPGe) crystal. Compared to other semiconductors like silicon, germanium has a high Z value which makes it a viable gamma spectrometer. Solid-state detectors offer the best energy resolution. However, one of the biggest drawbacks to solid-state detectors is the small band gap of the HPGe crystal. The detector needs to be cooled to prevent the creation of charge carriers through thermal excitation. The detector needs to be mounted in a vacuum chamber that is inserted into a Dewar with liquid nitrogen with

a temperature of around 77K. This makes the HPGe more expensive and less compact than scintillators and gas-filled detectors.



Figure 1. 7. Ontario tech U solid-state detector

1.3.2 Characteristics of Charge Particle Detectors

1.3.2.1 Charge Particle Spectroscopy

Charged particle spectroscopy, is a qualitative and quantitative method of identifying different radioisotopes by the emission of either beta particles or alphas during a decay. The activity or the intensity of the radiation can be determined by the count or the peak of the spectrum.

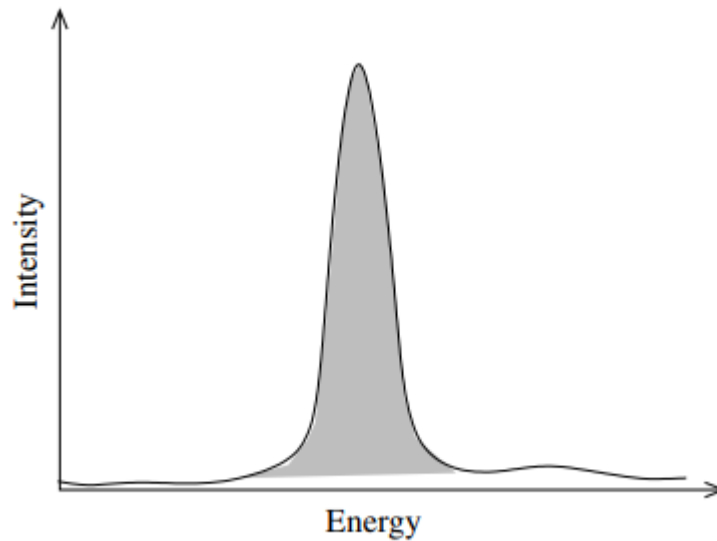


Figure 1. 8. Typical spectra for alpha particles. [2]

Unlike gamma-ray spectroscopy where there are multiple peaks because of the various gamma interactions, charged particle spectroscopy is simpler because the particle only deposits energy into the detector, creating an absorption peak.

An important aspect of charged particle detection, especially for heavy charged particles, is the range. If the scintillator crystal is too small, then higher energy particles pass through the crystal and do not provide accurate measurements of the energy of the particle. Therefore, determining the Bragg peak for heavy charged particles is important to understand the ranges of the particles at specific energies. Then designing the detector with these ranges in mind for charged particles [2,7].

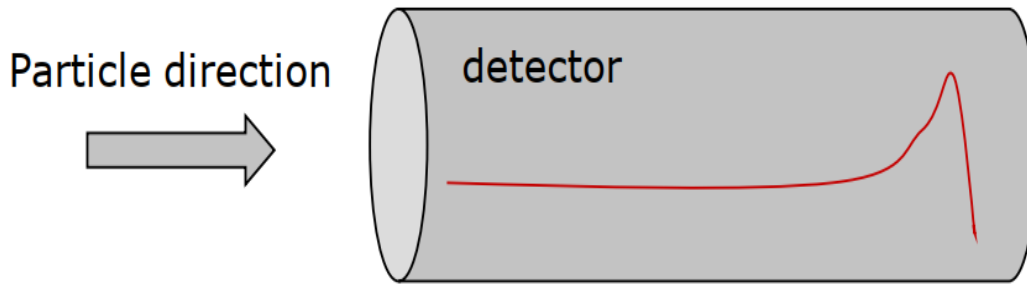


Figure 1. 9. Ideal energy deposition of a heavy charged particle in a detector

1.3.2.2 Energy Resolution

When a charged particle deposits all its energy into the detector, the signal should be processed into one channel creating a single line for the spectra. However, the pulse height spectra are spread across a band of channels of the multichannel analyzer (MCA) creating the peaks that are measured.

The energy resolution is the ability of the detector to differentiate or resolve two different peaks of differing energies. If the energy resolution of the detector is poor, then two different radiation sources with similar energies could be measured as one peak rather than two distinct peaks.

The energy resolution of the detector can be defined by the full width at half maxima of the defined peak of the spectra [2].

$$R = \frac{FWHM}{H_0} \quad (13)$$

Where:

FWHM = Full width at half maxima of the peak

H_0 = Peak energy (or channel) value

The energy resolution is expressed in a percent where lower percentages translate to more distinct peaks. Furthermore, the energy resolution decreases as the energy increases. The energy resolution of a detector depends on multiple factors: the intrinsic properties of the crystals, the type of the detector material, the electronics of the detector, and other factors all go into the resolution [2,7].

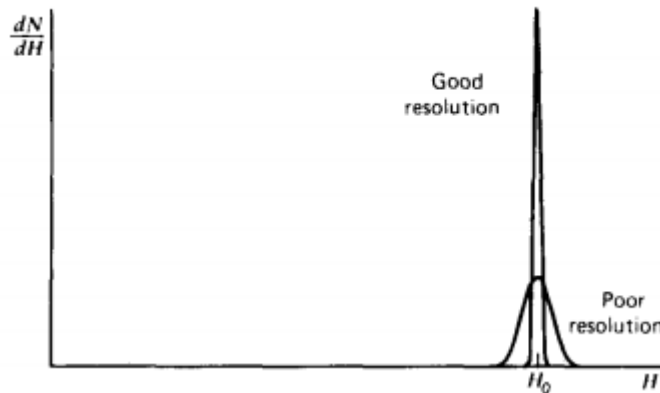


Figure 1. 10. Comparison between peaks with poor versus good resolution [5].

Figure 1.10 highlights how a detector with good resolution measures a peak in contrast to one with poor resolution. While both peaks are centered around the same energy, the peak with poor resolution has the counts spread across a wider range of channels resulting in a wider and smaller peak. Contrast this with the peak with good resolution, where most of the counts are binned in the same channel resulting in a larger narrow peak.

1.3.1.3 Efficiency

There are several classifications of detector efficiency. Detector efficiency is the ability to detect radiation with a defined type and energy. Comparing the radiation count detected to the true value of the number of particles or radiation. For neutral particles like gamma rays or neutrons, interactions with the detector can occur before detection. However, for charged particles, it either deposits part of or all of their energy [2,5].

There is absolute efficiency which is defined as:

$$\epsilon_a = \frac{\textit{number of pulses recorded}}{\textit{number of radiation quanta emitted by the source}} \quad (14)$$

One should consider that the absolute efficiency of a detector may not be useful to measure because not all the radiation quanta from the source reach the detector. An example is radiation sources that are isotropic emitting radiation from all directions. With these types of sources, the detector efficiency may become misleading. Intrinsic efficiency is more useful in these situations and is defined as:

$$\epsilon_i = \frac{\textit{number of pulses recorded}}{\textit{number of radiation quanta incident on the detector}} \quad (15)$$

This is a more meaningful definition of detector efficiency since it looks at the radiation that is only coming towards the detector, resulting in more accurate measurements of detector efficiency.

For isotropic sources, the two efficiencies can be related:

$$\epsilon_i = \epsilon_a \left(\frac{4\pi}{\Omega} \right) \quad (16)$$

- Ω is the solid angle of the detector from the actual source.

$$\Omega = \int_A \left(\frac{\cos\alpha}{r^2} \right) dA \quad (17)$$

- r is the distance between the source and detector surfaces
- α is the angle between normal to the detector surface and source directions
- dA is the detector surface element

For point sources located along the axis of a right cylindrical detector the solid angle can be calculated using this formula:

$$\Omega = 2\pi \left(1 - \frac{d}{\sqrt{d^2 + a^2}} \right) \quad (18)$$

Another definition of detector efficiency is the peak efficiency which is defined:

$$\epsilon_{ip} = \frac{\text{number of pulses recorded under the peak}}{\text{Number of pulses incident to the detector}} \quad (19)$$

The peak efficiency only looks at the radiation that deposits its full energy in the detector.

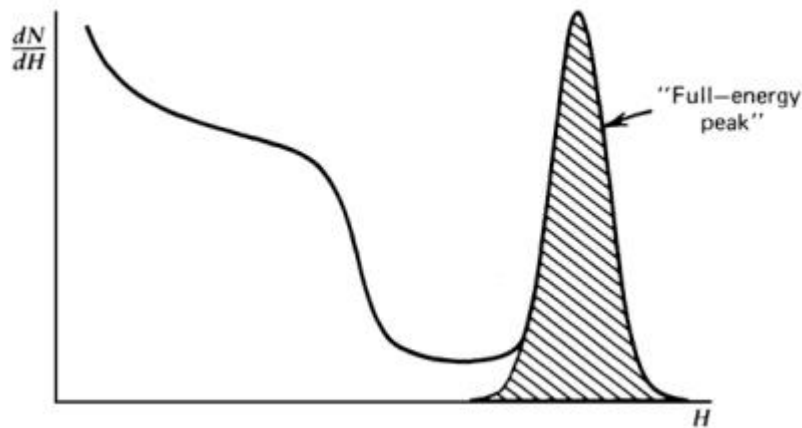


Figure 1. 11. Full energy peak for a spectrum [7]

1.3.1.4 Light Output

Light output is quantified by the number of photons produced by the scintillator material per unit of deposited energy of the radiation [5]. Light output affects the efficiency and the energy resolution of the detector. The light output of a scintillator is dependent on the type of particle or photon and the energy of the radiation. The light output of the scintillator material to ionizing radiation is also dependent on the stopping power (dE/dx). The idea behind this is that materials with high ionization density along the particle track reduce the overall scintillation, decreasing the light output. Factoring the stopping power for light output, it is quantified using this equation known as Birk's formula which is defined as:

$$\frac{dL}{dx} = A \frac{\frac{dE}{dx}}{1 + kB \frac{dE}{dx}} \quad (20)$$

- dL/dx is the light output per unit path length

- A is defined by the scintillator efficiency
- kB is defined as the Birks parameter in $\text{g cm}^{-2} \text{MeV}^{-1}$

To determine the total light output, the internal energy of an electron should account for all the light produced as the electron slows down. All the energy of the electron should be lost in the scintillator. Taking this into consideration, the total light output is the integration of the Birks formula [5,25]:

$$L(E) = \int_0^E \left(\frac{A}{1 + kB \frac{dE}{dx}} dE' \right) \quad (21)$$

- E is the initial energy of the electron in eVs

1.4 LaBr₃ Crystal

A considerable amount of research has been done on the LaBr₃ crystal. This crystal provides a direct upgrade in gamma-ray detection from the Sodium Iodide (NaI) crystal which has been the most prominent scintillator crystal for the application of gamma-ray detection. This section of the chapter outlines the research that has been put forward on the LaBr₃ crystal.

1.4.1 LaBr₃ crystal compared to other scintillator materials

The LaBr₃ crystal compared to the rest of the scintillator detectors offers the greatest energy resolution. This is due to the high light output which was measured at $\sim 63,000$ ph/MeV. This is the highest among the common scintillator detectors used. Furthermore, it has a fast decay time measured at 16 ns. These two factors contribute to the peak anode current. This is because they

directly affect the current that flows into the PMT, photocathode and dynode chain. This all is considered in the signal processing which forms the detection signal.

The anode peak current I_a for scintillator/PMT combinations can be expressed using this equation:

$$I_a = \frac{\text{Light output} * \text{Quantum Efficiency} * e * \text{Gain}}{\text{Decay Time}} \quad (22)$$

- e is the electric charge = $1.602 \cdot 10^{-19}$ C

Table 1.1 outlines and compares the anode peak current and other scintillator factors between the LaBr₃ detector and typical scintillator detectors. These values were measured for 1 MeV gamma radiation. From the table, it clearly outlines that the LaBr₃ detector excels in all metrics, especially in anode and photocathode current.

Table 1. 1 Comparison of LaBr₃ and the most common scintillator detectors for 1 MeV gamma-rays [21]

| | Wavelength max emission(n m) | Light Yield (ph/keV) | Decay time (ns) | Typical photocatho de QE (%) | Photocatho de current per absorbed MeV (uA) | Anode peak current (I_a) per absorbed MeV (mA) |
|-------------------------|---|-------------------------------------|--------------------------------|---|--|--|
| Na: TI | 415 | 38 | 250 | 30 | 0.0073 | 1.82 |
| CsI:Tl | 550 | 54 | 1000 | 7 | 0.0006 | 0.15 |
| CsI:Na | 420 | 41 | 630 | 30 | 0.0031 | 0.77 |
| CsI | 315 | 2 | 16 | 17 | 0.0034 | 0.85 (0.52) |
| BGO | 480 | 10 | 300 | 21 | 0.0011 | 0.28 |
| BaF ₂ (fast) | 220 | 1.8 | 0.8 | 1 | 0.0036 | 0.9 (0.07) |

| | | | | | | |
|-------------------------|-----|----|-----|----|--------|-------------|
| BaF ₂ (slow) | 330 | 10 | 630 | 15 | 0.0004 | 0.09 |
| LaCl ₃ : Ce | 350 | 49 | 28 | 27 | 0.0745 | 18.6 (13.7) |
| LaBr ₃ : Ce | 380 | 63 | 16 | 30 | 0.1890 | 47.3(29.1) |
| LYSO | 420 | 32 | 41 | 29 | 0.0368 | 9.21(7.4) |

Although these high instantaneous currents can be achieved in the detector, this comes with drawbacks. The detector is susceptible to signal saturation, in which an increase of energy from radiation does not correspond to a linear increase in the channel output in the signal processing. This presents a problem with calibrating the detector and measuring inaccurate values of energy in the pulse height spectra. In the literature, saturation was observed with protons ranging from 1-80 MeV.

A solution to this signal saturation is the evaluation of different PMT configurations. The literature describes two different configurations that have been assessed. The first configuration describes the standard dynode chain under bias. The second configuration is a 4-stage reduced chain. Figure 1.12 presents the schematic diagram of the two configurations.

Configuration 2 was successful in preventing the signal saturation over a wide range of energy while at the same time preserving the energy resolution. Although it was found that configuration 1 was satisfactory, especially with PMTs manufactured by Photonis [21].

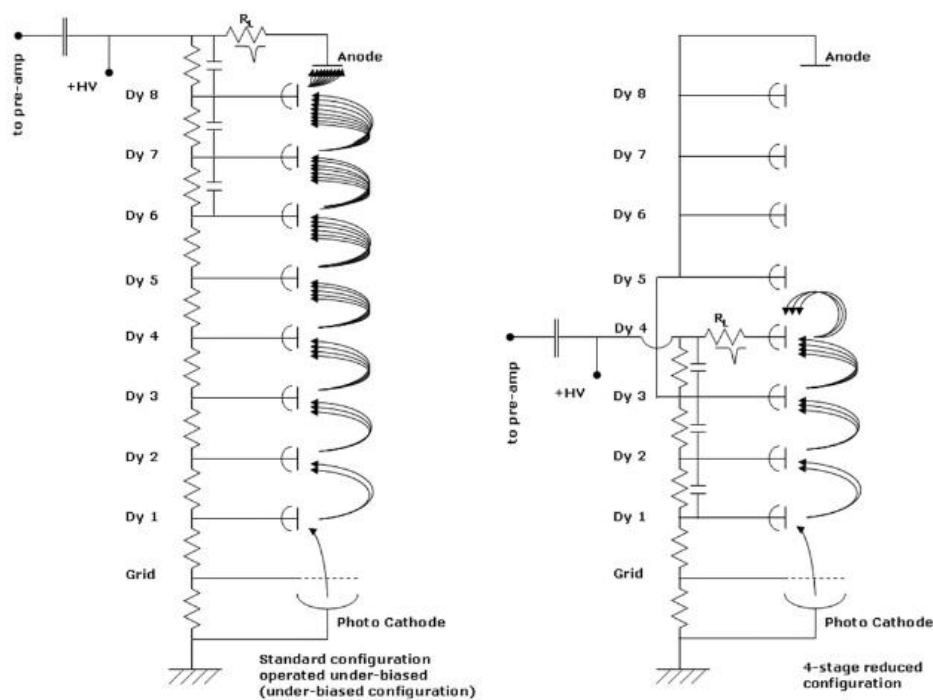


Figure 1.12. Schematic diagrams of the two PMT configurations Standard dynode chain (left) and 4-stage reduced chain (right) [21].

1.4.2 LaBr₃ crystal used in space missions

As shown above, the LaBr₃ crystal provides superior scintillator properties (light output, decay time, etc.). Furthermore, these detectors along with the properties stated above are proven to be essential in gamma radiation detection systems with limited resources and maintenance, which is common in interplanetary space missions. These scintillator detectors have been used in ESA's BepiColombo missions to Mercury in 2013 [9].

The LaBr₃ detector has been widely used in various space missions. First, compared to other common scintillator detectors, the LaBr₃ detector surpasses them in every scintillator metric as

shown in table 1.1 [9]. Next, is the reliability and robustness of the scintillator. It can be used reliably in the harsh environments of space without degradation in performance.

1.4.2.1 Problems with crystal growth

The initial production of the crystal presented problems when scaling the material, specifically when producing crystals a few cm³ larger. Problems presented with crystal crackling since the lanthanum halide crystals are anisotropic materials. The thermal conductivity and the thermal expansion coefficients vary with the main axis for the crystalline structure [9]. However, increasing the crystal sizes up to 3 x 4 inches for LaBr₃ and 4 x 6 inches for LaCl₃ without crackling have been achieved.

Following this, determining whether the resolution of the detector changes with increasing volume was investigated. The literature has shown that there is no change in energy resolution with increasing crystal volume, which is outlined in Table 1.2 [9.21].

Table 1. 2 Detector resolution with the increasing volume of the LaBr₃ crystal [21]

| Volume cm³ | Volume increase factor* | $\Delta E/E$ at 662 keV, % |
|------------------------------|--------------------------------|--|
| 0.90 | 1 | 3.2 |
| 1.73 | 1.9 | 3.4 |
| 5.39 | 6 | 3.4 |
| 12.27 | 14 | 2.8 |
| 43.10 | 48 | 2.8 |
| 103.0 | 114 | 3.0 |
| 155.2 | 172 | 3.0 |
| 347.5 | 386 | 2.8 |
| 462.7 | 514 | 3.0 |

***Volume increase factor is relative to the initial volume**

1.4.2.2 Energy Resolution and Crystal volume

Radiation detection systems intended for space need to be able to perform under environments with remarkably high energy radiation, like in a solar event. The detector should be able to work optimally even when it is exposed to radiation which can induce damage to the detector. The LaBr₃ radiation tolerance was evaluated with 200 MeV protons through a cyclotron in Groningen, Netherlands. Several LaBr₃ crystals were exposed to protons of varying fluences above the 60 MeV threshold. These crystals were exposed to fluences between 10⁹-10¹² protons cm⁻². The energy resolution, light output, and background count rate were measured before and after the irradiation to determine if there were any changes to the performance of the detector. What was found was that the background count of the detector increased, but there was no measurable difference in the energy resolution for all the crystals irradiated.

Table 1. 3 Various LaBr₃ detectors resolutions before and after proton irradiation [9]

| Before irradiation | | | | | |
|--------------------|----------------------------------|--------------|------|------|------|
| | | Energy (keV) | | | |
| Det no. | Fluence protons cm ⁻² | 60 | 662 | 1173 | 1332 |
| | | Resolution % | | | |
| J149 | 0 | 10.59 | 2.78 | 2.04 | 1.73 |
| J150 | 0 | 12.01 | 2.28 | 2.58 | 2.42 |
| J146 | 0 | 10.99 | 3.07 | 2.40 | 2.18 |
| J148 | 0 | 10.62 | 2.95 | 2.23 | 2.06 |
| J147 | 0 | 11.04 | 3.05 | 2.37 | 2.23 |

| After irradiation | | | | | |
|-------------------|-----------|-------|------|------|------|
| | | 60 | 662 | 1173 | 1332 |
| J149 | 0 | 10.26 | 2.52 | 1.76 | 1.63 |
| J150 | 10^9 | 12.10 | 2.80 | 2.16 | 1.97 |
| J146 | 10^{10} | 10.59 | 2.70 | 2.07 | 1.75 |
| J148 | 10^{11} | 11.51 | 2.75 | 1.85 | 1.79 |
| J147 | 10^{12} | 12.06 | 3.30 | 2.69 | 2.67 |

1.4.2.3 Crystal Activation with Prolonged Exposure

The count rates were measured after the irradiation of the crystals. This was to determine if the activation of crystals increased too much due to the flux of the beam. The background spectra were measured over 18.75 days. What was observed was that only when the fluence of the proton beam increased to 10^{12} protons cm^{-2} was there a significant increase in activation in the crystal [9].

1.4.3 LaBr₃ Detectors for Fission events

The sections above have shown that the LaBr₃ detectors are very proficient in gamma-ray detection and measurements. However, research has shown that the LaBr₃ detector can be used to obtain information about neutrons. This was done by having the gamma rays detected along with the fission fragments. The LaBr₃ detector allows for clean separation of gamma-rays in a time-of-flight configuration. This is possible due to the detector's excellent timing resolution to allow gamma-ray separation from the different processes of their creation.

These experiments were done on both Lanthanum detectors (LaBr₃ and LaCl₃). The experiment with the LaBr₃ detector was used for the measurement of the gamma-ray energy from a ²⁵²Cf

reaction. Poly-crystalline chemical vapor deposited (pcCVD) diamond detectors functioned as the fission trigger for the coincident measurements of the gamma-rays. It was found that gamma rays from prompt fissions were easy to differentiate from gamma rays induced by reactions with fast or slow neutrons. This is because there are various times of flight between neutrons and photons.

The ability to differentiate between the different neutron events allows for the extraction of information about the neutron spectrum. Furthermore, it can help obtain information like the cross-section of the material or spatial distribution [10].

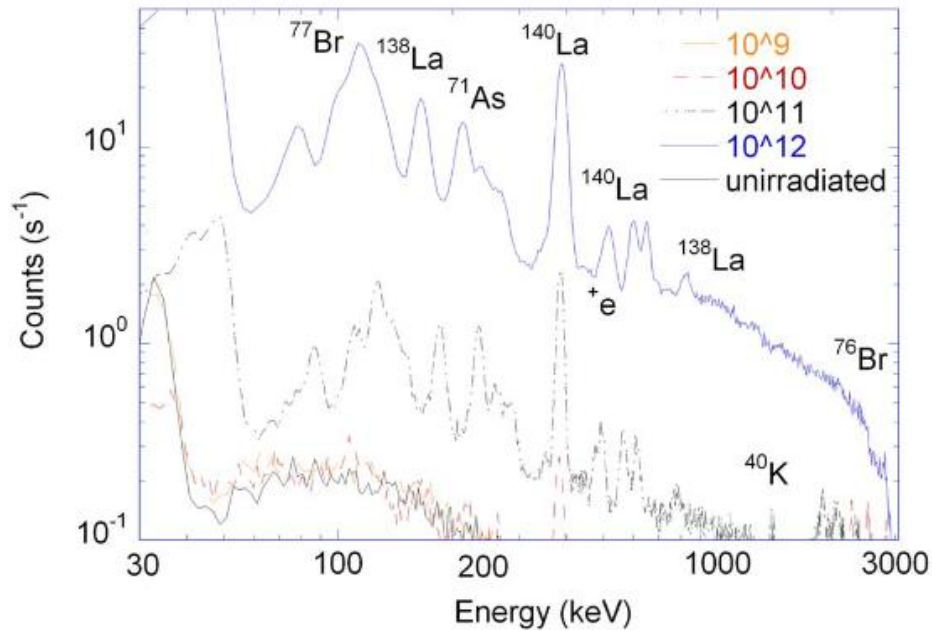


Figure 1.13 Activation of the LaBr₃ crystal with increasing proton flux [9]

1.4.4 Analytical expression for total and full energy peak efficiencies for LaBr₃: Ce Detectors

Work had been done in determining analytical expressions for the total and full energy peak efficiencies of the LaBr₃ detectors. Determining these allows for the calibration of the detector without the need for gamma sources. An accurate expression for the energy peaks requires two

factors to be considered. The first is the path length of the photon. Where their photon travels within the active volume of the detector. The second is the geometrical solid angle of the photon, which is the angle of entry of the photon [12].

A method for determining the path length of the photon in the crystal was obtained. The path length was found to be a function of the polar angle θ and the azimuthal angle ϕ . Two cases need to be considered when determining the photon path length. Where the photon enters the cylindrical detector material and leaves from either the cylindrical base (d_1) or the side of the cylinder material (d_2). Figure 1.13 outlines the possible path lengths of the source point through the detector. The path length d for each case can be determined with the following expression:

$$d_1 = \frac{L}{\cos\theta} \quad (23)$$

$$d_2 = \frac{M(\phi)}{\sin\theta} - \frac{h}{\cos\theta} \quad (24)$$

Where L is the length of the cylinder and h is the distance between the point source and the cylinder. $M(\phi)$ is the distance from the projection of the point source on the surface of the cylinder to any point of the circumference.

$$M(\phi) = -\rho\cos\phi + \sqrt{R^2 - \rho^2\phi} \quad (25)$$

Where ρ is the distance between the center of the cylinder base and the projection of the point source.

The total efficiency of the detector for a photon with a certain energy is derived as:

$$\epsilon_{point} = \frac{1}{2\pi} \int_0^\pi \left(\int_0^{\theta_1} f_1 d\theta + \int_0^{\theta_2} f_2 d\theta \right) d\phi \quad (26)$$

With,

$$\theta_1 = \tan^{-1} \left(\frac{M(\phi)}{h + L} \right) \quad (27)$$

$$\theta_2 = \tan^{-1} \left(\frac{M(\phi)}{h} \right) \quad (28)$$

$$f_i = f_{att} (1 - e^{-\mu d_i}) \sin\theta \quad (29)$$

In these equations, μ is the attenuation coefficient of the detector material and f_{att} factors determine the photon attenuation by the aluminum housing of the detector [12].

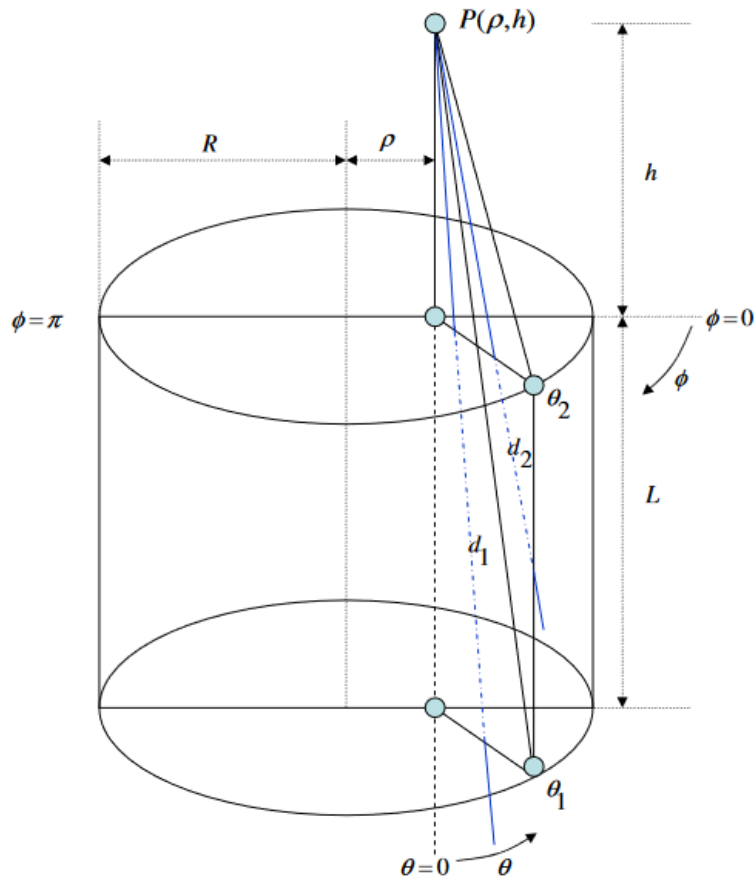


Figure 1. 14 View of all the photon path lengths through the scintillator material cylinder from a point source [12]

1.4.4 LaBr₃ Detectors in Portable Autonomous Radiation Detection

There has been work incorporating LaBr₃ detectors with semi-autonomous robots to minimize human interaction in areas of high doses of radiation, minimizing health risks induced from radiation. The focus of this was to provide a small, inexpensive method to measure and gather data in areas that may be too hazardous for humans to enter.

This was done by creating a program that calculated the counting efficiency of the detector, at the same time measuring the point source of the gamma radiation. Furthermore, a small prototype robot was constructed housing a LaBr₃ detector. This robot has two operational modes, one is a scan mode where it scans the local area, where it measures the intensity of the gamma-ray source, and determines the direction of the source. In the second mode, the robot moves toward the gamma-ray source through a rough 360-degree scan. This was achievable due to the good directional sensitivity of the LaBr₃ detector to measure the incidence angle of the gamma rays [13].

1.4.5 LaBr₃ Detector as an Environmental Radiation Monitor

Gas detectors are used for environmental radiation monitoring (ERM). This has its limitations where it can provide only the ambient dose rate around the detector chamber. LaBr₃ detectors are currently being used to measure real-time dose rates and radioactivity for gamma-ray nuclides. This was done by first subtracting the intrinsic background peaks of the detector. Then using a dose conversion factor, the gamma spectrum was used to determine the dose rate. Full absorption peaks from different gamma sources were analyzed to determine each dose rate for the measured gamma sources. It was found that an ERM system with a LaBr₃ can reliably measure and assess dose rate for gamma sources [14].

Chapter 2: Methodology Description

This chapter describes the methodology used in this study. The methodology consists of two parts: the first part is the simulation of the detector response to high energy He ions performed using Monte Carlo N-Particle Transport (MCNP). Specifically, MCNP/X (Monte Carlo N-Particle eXtended) version 2.6. The second part of the methodology covers the experimental investigation.

2.1. Modeling and Simulation

MCNP is code that was designed for the modeling and simulation of particle transport. This code was developed at the Los Alamos National Laboratory during the Manhattan Project. The base code has several transport modes which include neutrons, protons, electrons, and the coupling of those particles. The version used; MCNP/X allows for the transport simulation of 34 particles including numerous heavy ions.

This code remains a primary resource for simulating different situations using ionizing radiation. MCNP is still heavily used in nuclear transport, radiation protection, detector design, fusion/fission reactor design, nuclear medicine, and many more areas.

MCNP works by following individual particles from the source to the end of its path. Probability distributions are sampled using transport data, this is to determine the outcome of the particle at each step it travels. An example of this would be in figure 2.1 which outlines the outcomes of three different gamma photons. These gamma rays interact with the medium differently depending on the probability of the interactions. The more particles used, the better the probability distributions

are known for this interaction. These are then tallied with the statistical precision of the results [7,6].

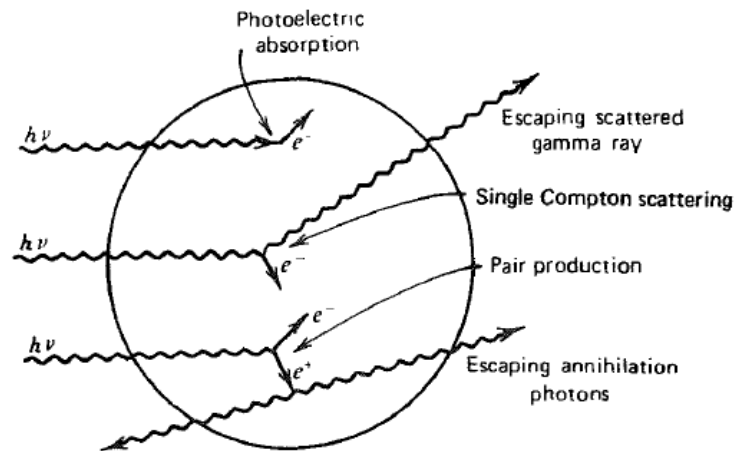


Figure 2. 1. Interaction using the gamma radiation to outline the possible outcomes through MCNP [15]

The tallied results are printed along with the relative error that is defined by one standard deviation of the mean over the estimated mean. This relative error is denoted as R. [16]

2.1.1 MCNP Input file

The input file is a text file that contains the inputs required to model the particle transport. An input file contains three blocks, each block has specific command lines that outline the modeling setup. These input lines define the geometry and material of the medium, the type of particle that travels through the geometry, the geometry of the source, and the type of tally used. The three different input blocks are as followed [15,16].

2.1.1.1 Cell block

This block defines any unions, intersects and/or complements between the surfaces of the volume or cell in the defined problem. Each line of the cell block contains these inputs in this order:

- **Cell number:** a number that is determined by the user, this number is arbitrary. Using numbers sequentially. Cannot exceed five digits
- **Material number:** Arbitrary number. This is zero if the cell is void.
- **Density:** Negative values are for mass density. Positive values indicate an atom density input. No values of density if this is a void.
- **Union/Intersection:** spaces between values indicate an intersection of cells. Colons indicate a union between cells
- **IMP:** The importance of a type of particle for the cell. This values either one or zero.

2.1.1.2 Surface Block

The user here defines the shape and the position in the shape of different surfaces. These surfaces can be planes or different shapes like spheres or cylinders. There are two ways to define surfaces here:

3. Providing the coefficients of the surface equations

The coefficients of the surface equations need to be assigned in the correct order. The surface cards are defined in this order:

- **Surface number:** arbitrary number chosen by the user.
- **Mnemonic:** the alphabetic mnemonic; this indicates the surface shape
- **Card Entries:** the coefficients for the surface equations

B. Providing Points that define a Surface

The surface can also be defined by inputting points in space of the surface with the corresponding surface mnemonics. An example of this would be:

| Surface Number | Mnemonic | Card Entries |
|----------------|----------|---|
| # | rcc | V _x V _y V _z H _x H _y H _z R |
| 1 | rcc | 0 0 0 0 0 10 5 |

- Rcc: right circular cylinder
- V_x V_y V_z: Coordinates along the center of the base
- H_x H_y H_z: a vector along the axis
- R: radius

Surfaces contain positive and negative sides. For example, a point defined on the surface of a sphere is negative. In the same vein, a point is defined outside the sphere. [17].

3.1.2.1 Data Block

This input block contains all the information on the modelling. This includes material specification and info, radiation source type, tallies specification.

- A) **Material Card:** Specific the composition and cross-section for all the cells containing a material number for the cell card. The material is defined by either atomic fraction or mass fraction.
- B) **Mode Card:** This defines the particle transportation mode. If the mode is not defined, then it is defaulted to set to N mode (neutrons)
- C) **Source Card:** This card defines the type of particle source, as well as the shape and position of the source. The source card defines different source parameters such as particle type, position in space, the shape of the source (point, circular, etc.), the energy of the source.
- D) **Tallies Card:** The tally card specifies what the model outputs as the simulation runs. This output can vary from measuring the current along the surface to measuring the pulse height at a certain cell. The tallies are defined by indicating a tally type which is a number from 1-8 and the particle type. These tallies are normalized to be measured per source particle. MCNP provides different cards that can be used in combination along with the tallies to get more tally information. For example, a card that can provide the relative error of the tally.

E) **Cut-Off Card:** Cut-off cards are used to shorten the execution time of the code. NPS is a cut-off card that ends the execution after a specified number of particles. The CTME card ends the code at the specified length of time.

F) **Print Card:** the output code can provide a table of information about the simulation. This print card can indicate what information to output or what information is turned off.

Table 2. 1 Different particles modes for base MNCP code [17]

| Mode | Description |
|-------------|--|
| N | Neutron transport only |
| N P | Neutron and neutron-induced photon transport |
| N P E | Neutron, neutron-induced photon and electron transport |
| P | Photon transport only |
| P E | Photon and electron transport |
| E | Electron transport only |
| N | Neutron transport only |
| N P | Neutron and neutron-induced photon transport |

Table 2. 2 Tally functions with the notations and a general description of the function [17]

| Tally Mnemonic | Description |
|------------------------|---|
| F1:N or F1:P or F1:E | Surface current |
| F2:N or F2:P or F2:E | Surface flux |
| F4:N or F4:P or F4:E | Track length estimate of cell flux |
| F5a:N or F5a:P | Flux at a point (point detector) |
| F6:N or F6:P or F6:N,P | Track length estimate of energy deposition |
| F7:N | Track length estimate of fission energy deposition |
| F8:P or F8:E or F8:P,E | Energy distribution of pulses created in a detector |

3.1.3 Geometric Simulation Model of LaBr₃ (Ce) Material

The LaBr₃ crystal was simulated using MCNP/X to determine the response function of the detector to He ions. The simulation followed the same manufactured dimensions, a 38.1 x 38.1 mm cylindrical crystal. The simulation used 10⁶ particles to reduce the statistical error in the results. The detector resolution was set to 2.0% in the code, using the Gaussian Energy Boarding (GEB) card which allows the simulation to consider the detector resolution of the crystal. Figure 2.2 is the 3-D view of the LaBr₃ crystal model used in the simulations.

2.1.2.1 MCNP/X Visual Editor

Normally, MCNP code is done using a text line editor as the input file for the simulations. The problem with this is that using the line editor alone is prone to more errors. This is also tedious due to all the different descriptions and definitions for geometries, tally outputs, and source parameters. These input text files could be thousands of lines and keeping up with all the parameters is cumbersome and difficult. Furthermore, it could take considerable time to assess geometries and correct any errors in the code.

To address this, a visual edition was developed for the code's input file. This visual editor was first developed in 1992 and the first build was released in 1997. Since then, MCNP has been released with the visual editor as a package starting at version 5 of MCNP. The visual editor allows the user to seamlessly input the surface geometry and to directly view the modelling information in the visual window as the user inputs the code [16,17,18].

Additional powerful features include [18]:

- Two side-by-side 2-D plots of the geometry.
- Capability to plot source points to verify the MCNP/MCNPX source.
- Optional 3-D views using either ray tracing or dynamic wire mesh displays.
- Capability to dynamically build geometry while viewing it as it evolves.
- Optional manual editing of the input file and immediate re-initialization with the changes showing up in the plots.
- Dynamic input of materials, transformations, and importance (using the mouse).
- Dynamic displays of particle tracks, cross-sections, and tallies.
- A surface wizard to optionally assist the user in creating surfaces while visually being able to see the surface types.
- A cell wizard to assist the user in creating cells.
- Optional import and conversions of a CAD file to an MCNP/MCNPX input file

The code for the simulation is created using the visual editor software. Taking advantage of the 2-D plots and the 3-D view mode. Furthermore, the ability to dynamically change factors like the materials, importance, and the geometries then view the changes immediately made the construction of the simulation more streamlined.

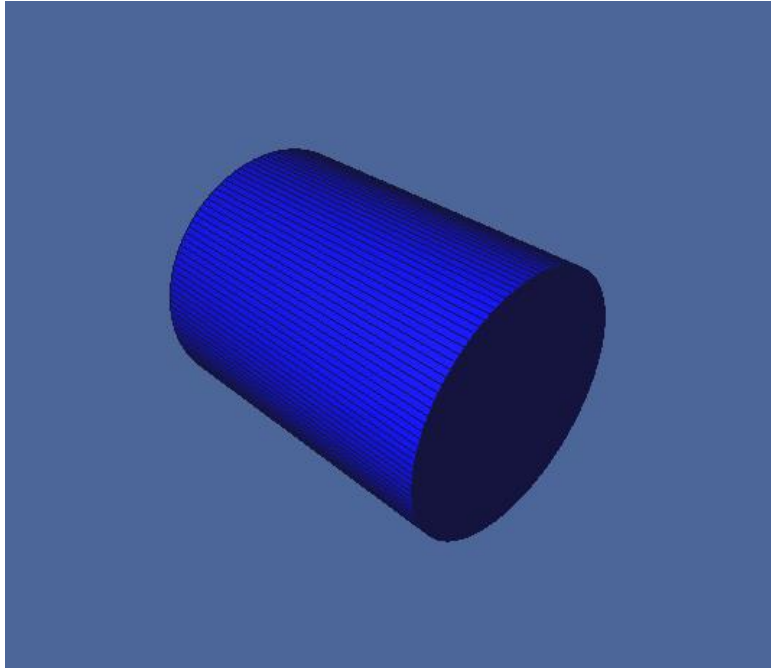


Figure 2. 2. 3-D view of LaBr₃ crystal with the MCNP/X code

2.1.2 Stopping Power and Ranges of Ions in Matter Table

The Stopping Power and Ranges of Ions in Matter (SRIM) software are programs that calculate the stopping power and ranges of ions, up to 2 GeV/amu. These calculations are done using the quantum mechanical models of ion to atom collisions. During the collisions, the ions and atoms interact via Coulomb collisions, with exchange and correlation interactions between the electron shells [19].

The screenshot shows the SRIM software interface for creating a table. The window title is "Ion Stopping & Range Tables". The main area is divided into sections for "Ion" and "Target" input. The "Ion" section includes fields for Symbol (PT), Name (H), Atomic Number (1), and Mass (1.008). The "Ion Energy Range (keV)" is set from 10 to 10000. The "Target" section includes a Target Description field (Target), Density (g/cm3), and Gas Tgt. checkbox. Below these are buttons for "Add Element", "Compound Dictionary", and "Restore Last Target". A table for adding elements is visible with columns: Delete Element, Symbol, Name, Atomic Number, Weight (amu), Stoich, and Atgm %. The table currently has one row with Symbol "PT", Atomic Number "0", Stoich "1", and Atgm % "100%". At the bottom, there are "Stopping Power Units" (MeV / (mg/cm2)), "Compound Correction" (1), and a set of control buttons: "Calculate Table" (green), "Clear All" (orange), "Main Menu" (light blue), "Quit" (red), and "Problem Solving" (green).

Figure 2. 3. SRIM table input window

SRIM provides a table of values for specific ions and target atoms. The output window allows the specification of the desired ion and energy. In addition, it allows the user to specific target molecules along with the density. It also contains a compound dictionary with various materials with their corresponding densities. Figure 2.3 displays the SRIM table input window.

| Ion Energy | dE/dx Elec. | dE/dx Nuclear | Projected Range | Longitudinal Straggling | Lateral Straggling |
|------------|-------------|---------------|-----------------|-------------------------|--------------------|
| 100.00 MeV | 8.809E+00 | 4.763E-03 | 6.26 mm | 278.14 um | 84.19 um |
| 110.00 MeV | 8.150E+00 | 4.366E-03 | 7.43 mm | 325.13 um | 99.64 um |
| 120.00 MeV | 7.592E+00 | 4.032E-03 | 8.71 mm | 372.35 um | 116.22 um |
| 130.00 MeV | 7.113E+00 | 3.748E-03 | 10.07 mm | 420.03 um | 133.90 um |
| 140.00 MeV | 6.698E+00 | 3.502E-03 | 11.51 mm | 468.30 um | 152.66 um |
| 150.00 MeV | 6.334E+00 | 3.288E-03 | 13.05 mm | 517.22 um | 172.47 um |
| 160.00 MeV | 6.012E+00 | 3.100E-03 | 14.67 mm | 566.84 um | 193.32 um |
| 170.00 MeV | 5.726E+00 | 2.932E-03 | 16.37 mm | 617.15 um | 215.18 um |
| 180.00 MeV | 5.469E+00 | 2.783E-03 | 18.16 mm | 668.17 um | 238.04 um |
| 200.00 MeV | 5.027E+00 | 2.526E-03 | 21.97 mm | 861.17 um | 286.70 um |
| 225.00 MeV | 4.578E+00 | 2.268E-03 | 27.18 mm | 1.14 mm | 352.83 um |
| 250.00 MeV | 4.213E+00 | 2.058E-03 | 32.87 mm | 1.40 mm | 424.63 um |
| 275.00 MeV | 3.910E+00 | 1.886E-03 | 39.03 mm | 1.65 mm | 501.88 um |
| 300.00 MeV | 3.655E+00 | 1.741E-03 | 45.64 mm | 1.90 mm | 584.37 um |
| 325.00 MeV | 3.437E+00 | 1.617E-03 | 52.69 mm | 2.15 mm | 671.90 um |
| 350.00 MeV | 3.248E+00 | 1.511E-03 | 60.17 mm | 2.40 mm | 764.29 um |
| 375.00 MeV | 3.083E+00 | 1.418E-03 | 68.06 mm | 2.65 mm | 861.38 um |
| 400.00 MeV | 2.938E+00 | 1.336E-03 | 76.36 mm | 2.90 mm | 963.00 um |
| 450.00 MeV | 2.693E+00 | 1.198E-03 | 94.14 mm | 3.85 mm | 1.18 mm |
| 500.00 MeV | 2.495E+00 | 1.087E-03 | 113.42 mm | 4.73 mm | 1.41 mm |
| 550.00 MeV | 2.331E+00 | 9.956E-04 | 134.15 mm | 5.57 mm | 1.66 mm |
| 581.40 MeV | 2.244E+00 | 9.458E-04 | 147.87 mm | 5.91 mm | 1.82 mm |

Figure 2. 4. SRIM output table

The output produces a table of different values for the ion. It provides the electron and nuclear stopping power, the projected range, and longitudinal and lateral straggling of the ion in the target for a range of energy up until the specified maximum energy [19].

2.2 Experimental Study

The scintillator material used is a Lanthanum Bromide crystal ($\text{LaBr}_3(\text{Ce})$) housed in a hermetically sealed aluminum housing and mounted to a photomultiplier tube, an internal magnetic/light shield, and a 14-pin connector. The PMT that was paired with the scintillator is the Canberra model 2007. The detector was coupled with the Osprey ® MCA which is an all-in-one device that was developed by Canberra. The Osprey contains an HPVS, preamplifier, and a digital MCA. The detector can be connected to a computer using the MCA via USB. From there, pulse height spectra could be measured using data analysis software coupled with the MCA.

2.2.1. Lanthanum Bromide Detector Characteristics

The $\text{LaBr}_3(\text{Ce})$ crystal is cylindrical in structure. It has a high density of 5.08 g/cm^3 , in comparison, the density of NaI crystal is 3.67 g/cm^3 . The melting point of the crystal is 783 C , the crystal is highly hygroscopic and water-soluble. The LaBr_3 crystal is activated using cerium (Ce) to enhance the light output of the crystal. Table 2.3 outlines all the notable properties of the $\text{LaBr}_3(\text{Ce})$ crystal. [6]

Table 2.4 compares the scintillator properties of the NaI crystal to the $\text{LaBr}_3(\text{Ce})$ crystal. From the comparison, the $\text{LaBr}_3(\text{Ce})$ crystal has superior scintillator properties, yielding high light output per unit energy, faster decay times, and a lower peak emission wavelength (UV range) [6, 20].



Figure 2. 5. LaBr₃ detector along with the photomultiplier tube attached to the MCA

Table 2. 3. Physical Characteristics of LaBr₃(Ce) [6]

| Properties | Value |
|---|----------------|
| Density (g/cm ³) | 5.08 |
| Melting Point (°C) | 783 |
| Thermal expansion coefficient (10 ⁻⁶ /C) | 8 along C-axis |
| Cleavage plane | 100 |
| Refraction index at emission max | 1.9 |

Table 2. 4. Comparison of LaBr₃ (Ce) properties with NaI (TI) [6]

| Crystal | Density g/cm³ | Light Yield (photons/keV) | Decay time(ns) | Peak emission wavelength(nm) |
|------------------------|-------------------------------------|--------------------------------------|---------------------------|---|
| LaBr ₃ (Ce) | 5.1 | 65 | 16 | 380 |
| NaI(TI) | 3.7 | 39 | 250 | 415 |

The crystal was also designed to be robust and it has been evaluated to withstand about 100g shock, 30 g of random vibrations, and survive about 200 C temperatures. This makes the detector versatile, having the ability to be used in a wide range of environments.

One of the main advantages of the LaBr₃(Ce) crystal over NaI is the radiation resistance. This is especially useful for areas with extremely high radiation fluxes like space environments where high fluxes of protons and gamma radiation are found. According to Saint-Gobain the manufacturer of the scintillator crystal, after the LaBr₃(Ce) crystal has been irradiated by 1kGy of Co-60 the light output drops around 8% and the pulse height resolution worsens from 3% to 3.8%. However, it has been shown that the rate of degradation in performance by the scintillator is slow and performs optimally even up to and after doses past 111kGy [6, 22].

At room temperature, the light output of the LaBr₃(Ce) crystal outperforms the NaI (TI) crystal by 160%. As the temperature increases, the light output proportionally increases as well, having significantly greater light output compared to NaI (TI) [6,20,22].

The most important advantage of the LaBr₃(Ce) crystal over NaI(TI) is the greater energy resolution for the pulse height spectra [6,20]. This is important in the instances where detecting

and identifying multiple radiation sources is of concern. An example of this would be in radiation security where it is important to identify highly enriched U-235 in the presence of extremely high background. An additional feature to note about the $\text{LaBr}_3(\text{Ce})$ crystal is that it emits a natural 1434 keV Lanthanum peak since the isotope of lanthanum is a natural gamma emitter. The drawback to this fact is that radioisotopes that emit radiation in that energy range are hard to detect because of this natural peak, an example of this is K-40 which emits a 1461 keV gamma which is indistinguishable from the lanthanum peak.

2.2.1.1 Photomultiplier Tube

A 50.8 mm Hamamatsu R6231 PMT was used with the scintillator crystal. This is a head-on type PMT with a tube size diameter of 51 mm. It uses a Baikal photocathode, with a spectral response range of 300-650nm wavelength, with a quantum efficiency of around 27% at the peak wavelength of 240 nm. This spectrum range matches the emission spectrum of the LaBr_3 crystal which emits UV photons. Figure 2.6 shows the Hamamatsu R6231 PMT with a detailed diagram [33].

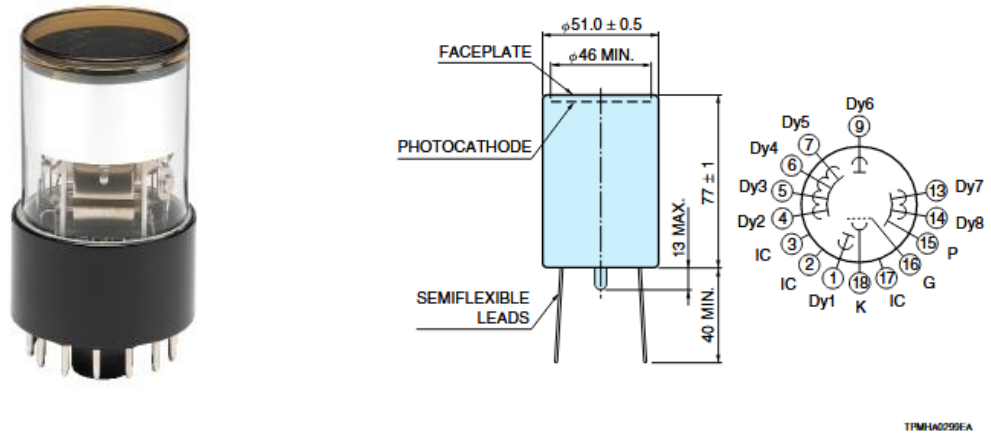


Figure 2. 6 Image of the Hamamatsu R6231 PMT (left) and the diagram with the dynodes outlines (right) [33]

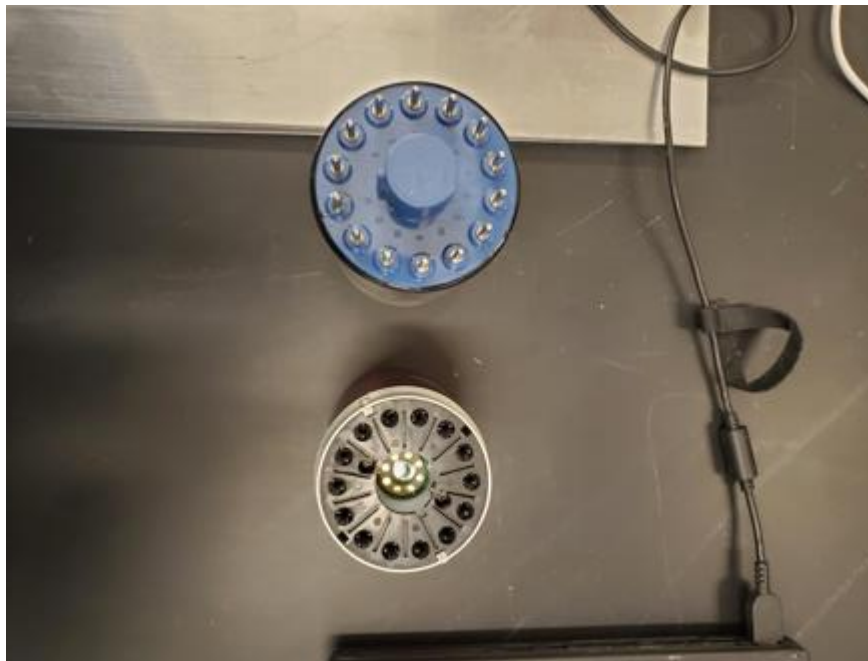


Figure 2. 7. Top-down view of the PMT

The overall performance of the PMT depends on several factors. The material used for the faceplate (light window), the material of the photocathode, the number and arrangements of the dynodes affect the overall performance of a PMT.

2.2.1.2 Window material

The window material determines the spectral range for photon transmission. The materials that can be used to produce the window can be borosilicate glass, UV-transmitting glass, quartz, or magnesium fluoride. In the case of the Hamamatsu R6231 PMT, it uses borosilicate glass. Borosilicate glass is used for gamma detection where most inorganic scintillation materials emit photons in the UV range (~300nm range). In the case of LaBr₃ (Ce), it emits UV rays with 380 nm wavelength [26].

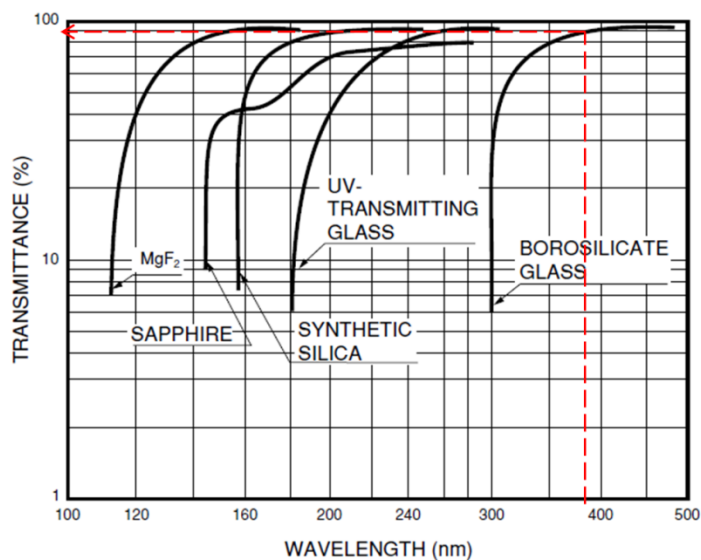


Figure 2. 8. Quantum efficiencies of different photocathode materials [33]

2.2.1.3 Photocathode Material

An important criterion for deciding on the photocathode material is the work function. The work function is the energy required by the photon to liberate an electron from the given material. The important characteristic for photocathodes is having a low work function. Many different metals can be used for the photocathode depending on the type of application of the detector. The Hamamatsu R6231 uses bialkali material (Sb-Rb-Cs, Sb-K-Cs), which provides the highest quantum efficiency at around 27%. The following figure compares the quantum efficiencies for varied materials [30, 33].

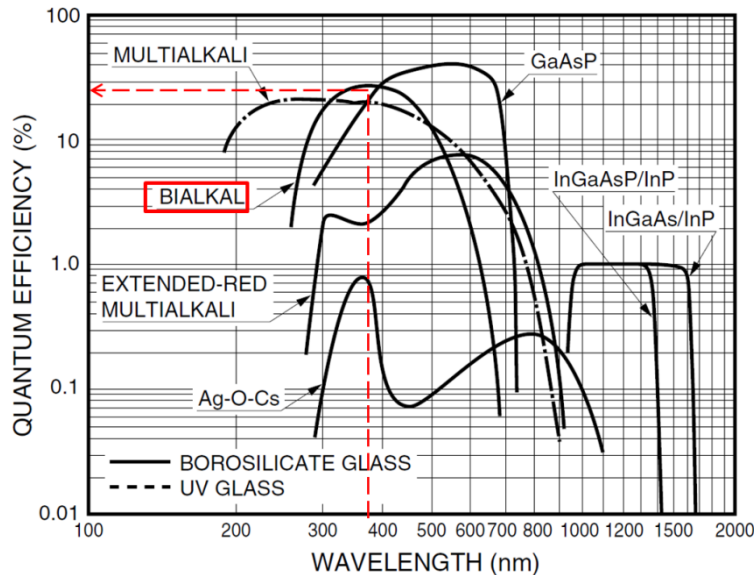


Figure 2. 9. Quantum Efficiency of varied materials in the PMT window [33]

2.2.1.4 Multichannel Analyzer

The MCA used in this study is the Canberra Osprey Universal MCA. This is an all-in-one device that contains a high voltage power supply (HVPS), preamplifier, and a digital MCA. The Osprey MCA can be controlled through either USB or ethernet without the need to use the two separate units which is usually the case. The MCA offers up to 2048 channels. The MCA identifies the arriving signal pulse and measures the energy and arrival time. Using this information, the MCA performs pulse shape analysis. The Osprey has several gain settings. x1, x2, x4 and x8 for coarse gain settings; x1-x5 for fine gain settings. Furthermore, users can adjust the high voltage over a wide range, outputting 0-1300V of high voltage settings [35].

2.2.2. Detector Calibration

Detectors need to be calibrated to read accurate pulse-height energy measurements. Detectors do not output energy values for pulse height spectrum measurements. The MCA bins each signal pulse into individual channels. The higher the channel the pulse gets binned in, the higher the energy of the source. To convert the channels into energy values, the detector needs to be calibrated using radioisotopes with known energy values. Using the calibration sources, a calibration curve can be obtained which then converts the channels into energy values in the spectrum [23,26,29].

Table 2.5 outlines various sources that were used to calibrate the detector, all the sources outlined were used at 37000 Bq. The detector was adjusted down to a high voltage value of 250V, for reference, the typical operating voltages are set to 750-1000V. This was done to account for anode

peak current when measuring high-intensity heavy ions. As mentioned previously, a natural lanthanum peak emerges in the spectrum. This peak was used in the calibration as well. Figure 2.11 shows the lanthanum peak through a measured background count lasting 12 hours.

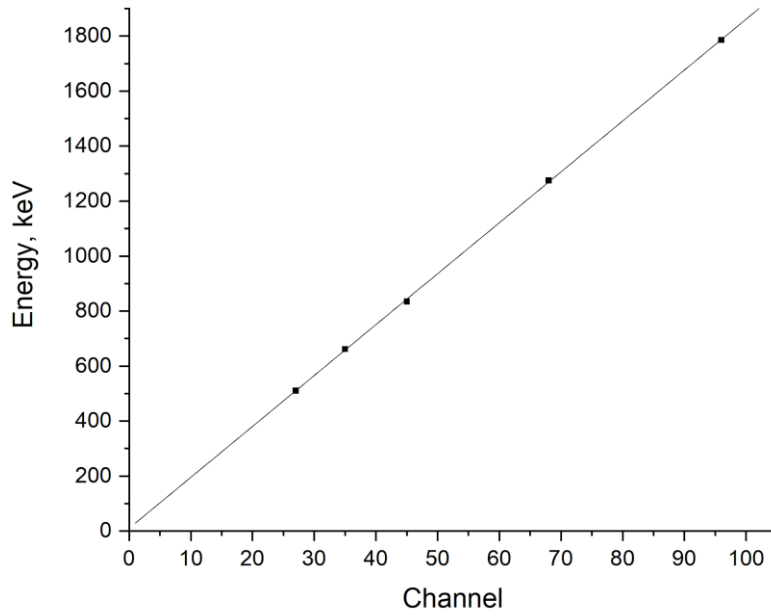


Figure 2. 10. Calibration curve of the LaBr₃(Ce) detector

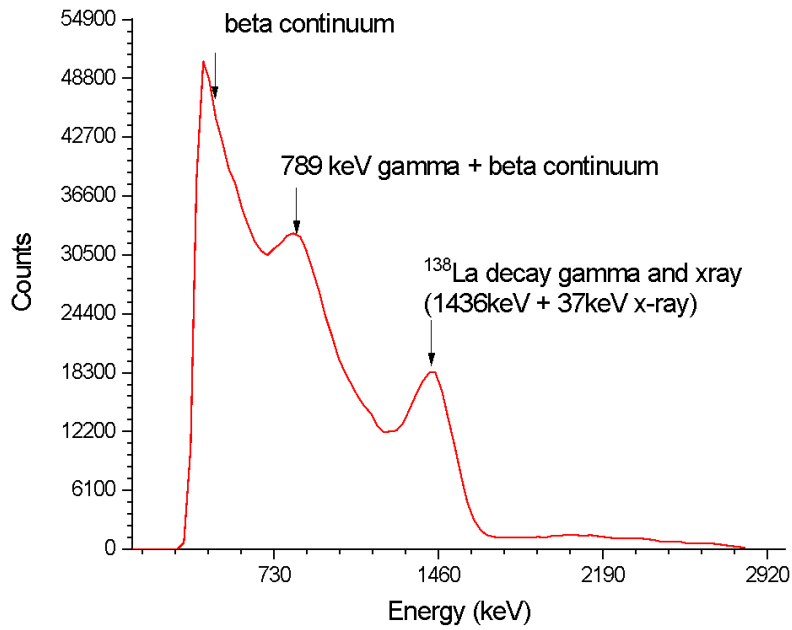


Figure 2. 11. 12-hour background count outlining the natural La peak

Table 2. 5 Radionuclide sources used for the detector calibration [34].

| Source | Activity, μCi | Half-life | Energy (MeV) |
|--------|--------------------------|-----------|--------------|
| Co-60 | 1 | 5.27 y | 1.173, 1.333 |
| Mn-54 | 1 | 313 d | 0.835 |
| Na-22 | 1 | 2.6 y | 0.511, 1.275 |

2.2.3. Experimental Setup and Facility

The experiment was conducted at the National Institute of Radiological Sciences (NIRS) in Chiba, Japan. The NIRS houses a linear accelerator, Heavy Ion Medical Accelerator in Chiba (HIMAC). The HIMAC is primarily used for cancer therapy. The facility is unique compared to other medical accelerators because it can accelerate several different heavy ions (H, He, C, O, Ne, Ar, Fe, Kr, and Xe). It can accelerate these heavy ions to exceedingly high energies, from 100 - 800 MeV/u depending on the ion. The HIMAC facility has several different exposure rooms within. One room is used for the direct beam for physics, another room contains a secondary beam for other experiments. In this study, the experimental measurements were taken in the biological room in the HIMAC facility. The biological room was used since it provides experiments and studies that require a wide and uniform beam setup [36].

Measurements of the detector responses were conducted using 150 MeV/nucleon He ions. The beam provided a 10 cm diameter mono-energetic heavy-ion beam. The beam energy was reduced to take multiple measurements at different energies using blocks of polymethyl methacrylate (PMMA) or 'binary filters (BF)' of varying thickness to control the energy of the heavy-ion beam.

The dose depth curve was determined using a PTW 23343 Markus Ion Chamber at different thicknesses of the BF. This was done to determine the initial energy of the heavy-ion beam.

The LaBr₃ detector was exposed to fluences that ranged from 20-100 particles cm⁻² s⁻¹. These fluences were used to minimize the dead time of the detector. The dead time for the detector ranged from 0.1-1.1% across all the experiments taken. The detector was irradiated by the beam for 3 minutes for each binary filter used. The total fluence was measured using a plastic scintillator between the beam and the detector. A background measurement was taken outside the HIMAC facility, this measurement was 12 hours long. Figure 2.9 shows the experimental setup along with the picture of the setup at the HIMAC facility. Figure 2.10 is a simple diagram of how the experiment was conducted.

The energy of the beam coming out of the BFs is calculated using the SRIM software described previously. An example of the calculation is found in appendix C.

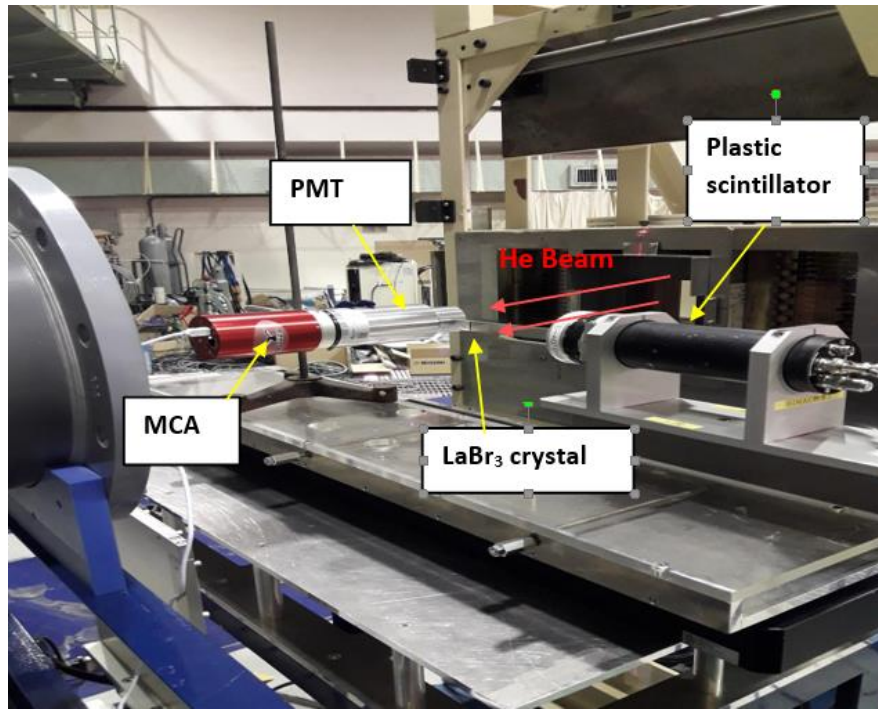


Figure 2. 12 Experimental Setup at HIMAC facility

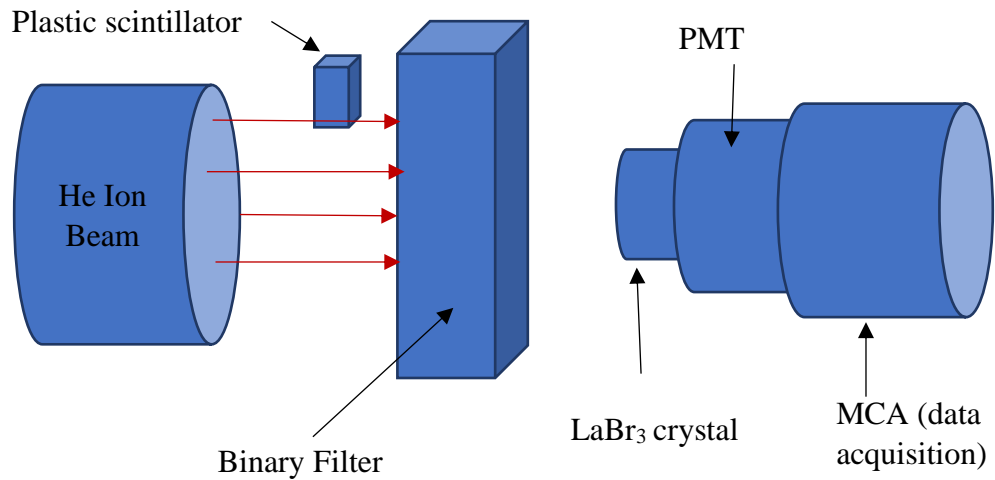


Figure 2. 13. Diagram of the experimental setup

2.2.4 Dose Depth Curve

Although the HIMAC beam can output 150 MeV per nucleon, the initial energy of the beam needs to be determined. This was done by measuring the dose depth curve of the binary filter. This curve was recorded using the Markus Ion chamber. Along with the SRIM table to determine the beam energy with the corresponding range it traveled in the binary filter. Figure 2.11 presents the dose curve to determine the range of the alpha beam and consequently the initial energy of the beam.

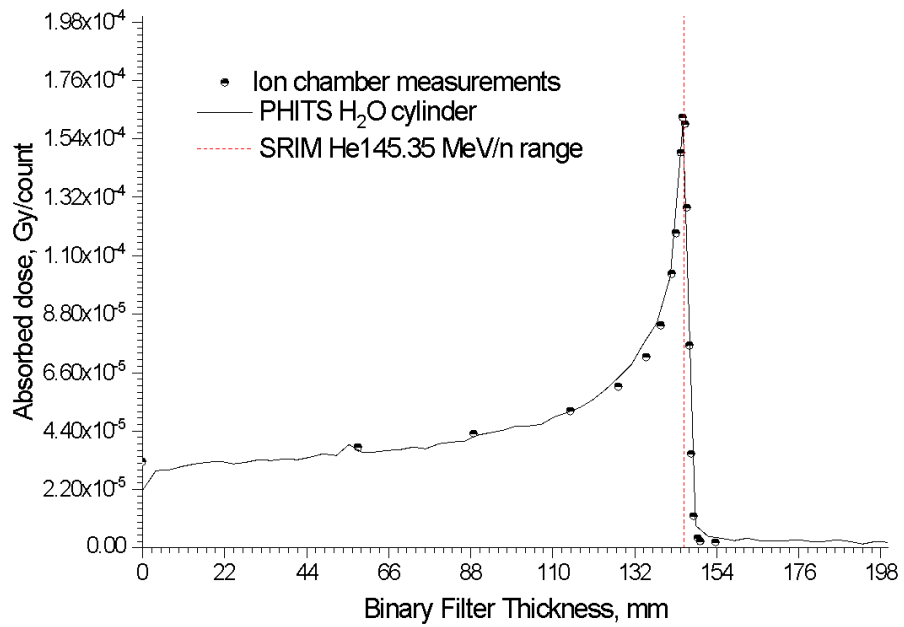


Figure 2. 14. Dose Depth Curve of the HIMAC He Ion Beam

Chapter 3: Results, Analysis, and Discussion

In the HIMAC facility biological room, several experiments have been performed using a wide range of thicknesses of binary filters, and MCNP/X code was used to simulate the detector response function. This section presents the results of the simulations as well as experiments. Both sets of data are analyzed.

3.1 Simulation Results

Figures 3.1-3.5 show the pulse height spectra from the MCNP/X simulation and the experimental data. The binary filters were simulated from 0mm – 143.16 mm thicknesses and the resolution of the detector was set to 2%, remaining consistent through all the simulations. The abscissa in MCNP/X spectra is the count per source particle. The pulse height spectra obtained for 0 mm – 40.03 mm demonstrates an increase in the deposited energy in the crystal. Past 40 mm, the deposited energy in the crystal decreases.

3.2 Experimental Results

Similarly, the experimental data is measured with the binary filters from 0 mm – 143.16 mm. The experimental spectra from figures 3.1-3.5 have been normalized to highlight the energies. From 0 – 40.03 mm, there is an increase in the deposited energy. Past 40.03 mm, the deposited energy inside the crystal decreases with increasing BF thickness. The detector resolution degrades significantly past 120.18 mm (lower beam energies).

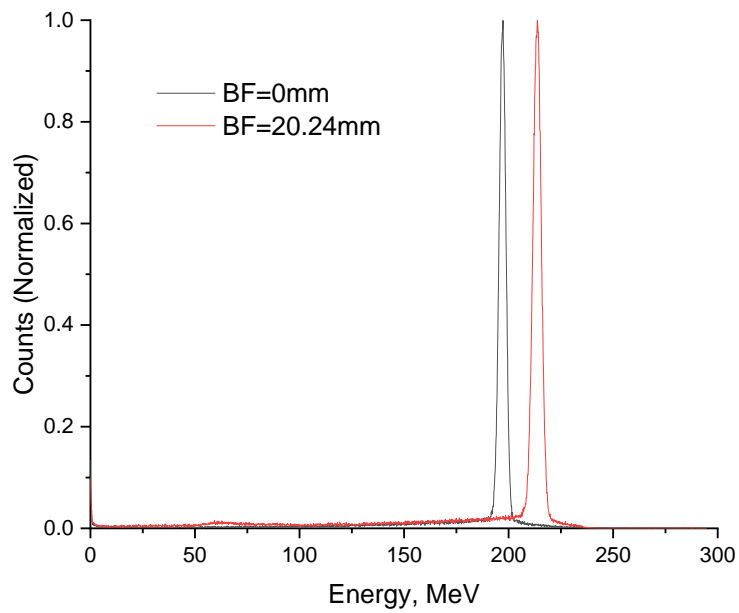
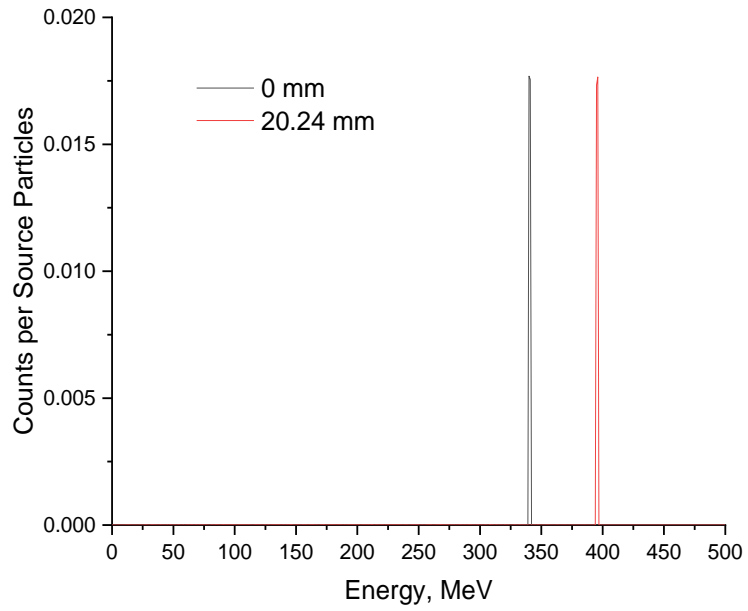


Figure 3. 1 Pulse Height Spectra of the MCNP/X simulation (top) and the experimental data (bottom) for 0mm and 20.24 mm BF

3.3 Comparison Between Experimental Data and Simulation

Figure 3.1-3.5 compares the pulse height spectra obtained between the MCNP/X simulations and the experimental results for numerous BFs.

Figure 3.1 reveals two peaks in the pulse height spectra corresponding to the BF at 0 mm and 20.24 mm for both MCNP/X (top) and experimental (bottom) data. The MCNP/X results show that for 0 mm and 20.24 mm, 340 MeV and 395 MeV are deposited into the crystal, respectively. Experimental data shows that at 0 mm and 20.24 mm, the beam deposits 198 MeV and 214 MeV, respectively. From the energies indicated from both spectra, the full energy of the He ions is not deposited in the crystal.

The spectra in figure 3.2 present two peaks for the BF at 40.03 mm and 60.32 mm for both the MCNP/X simulation and the experimental data. The beam deposits 474 MeV and 420 MeV, respectively. However, in the experimental results, the beam deposits 230 MeV and 216 MeV into the crystal, respectively. From this point past 40.03 mm, the full He ion energies are deposited into the crystal for both spectra.

Figure 3.3 is the pulse height spectra corresponding to 70.22 mm and 90.05 mm BF. The MCNP/X results indicate that the He Ion beam deposits 390 MeV and 328 MeV, respectively, in the crystal. However, experimental data shows that the beam imparts 210 MeV and 190 MeV of energy into the crystal.

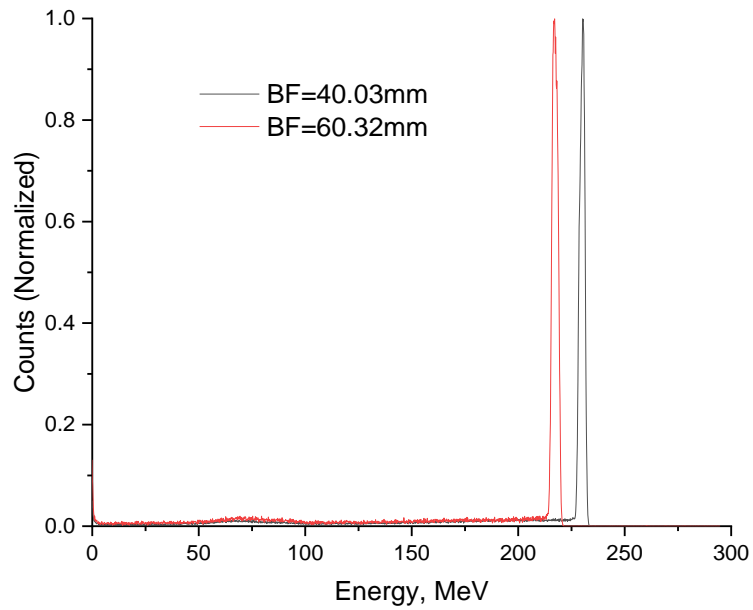
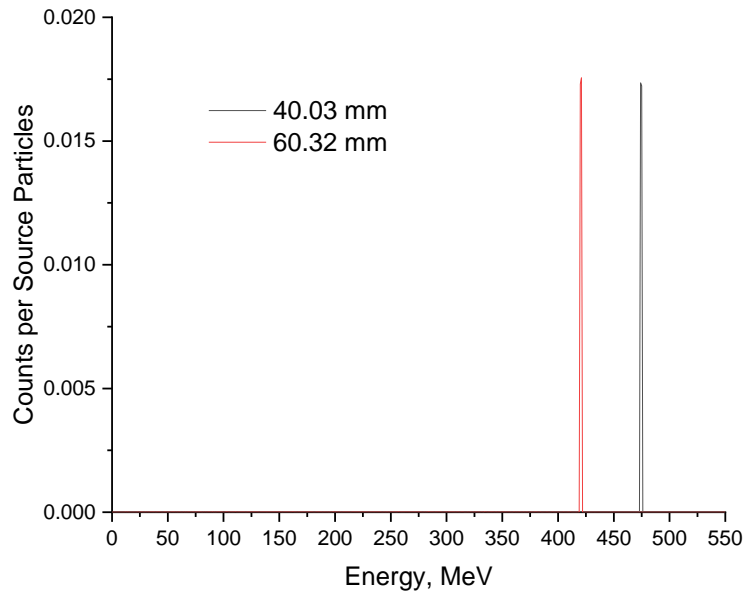


Figure 3. 2 Pulse Height Spectra of the MCNP/X simulation (top) and the experimental data (bottom) for 40.03mm and 60.32 mm BF

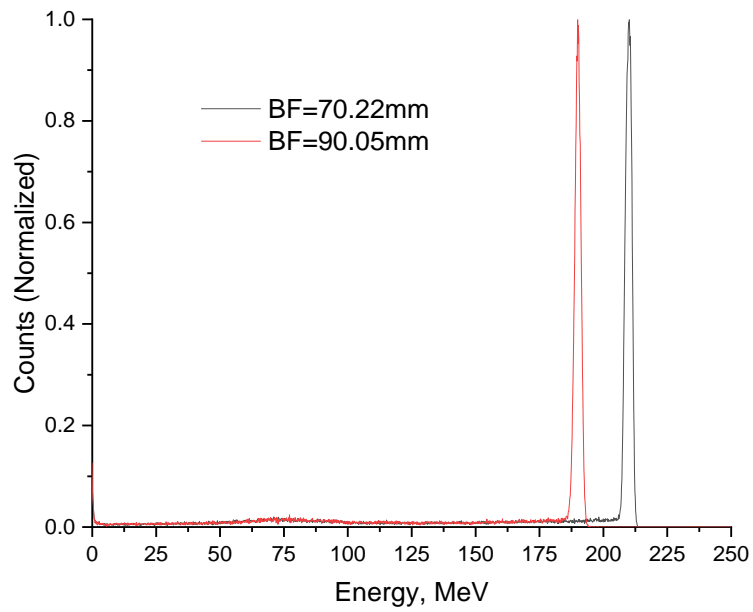
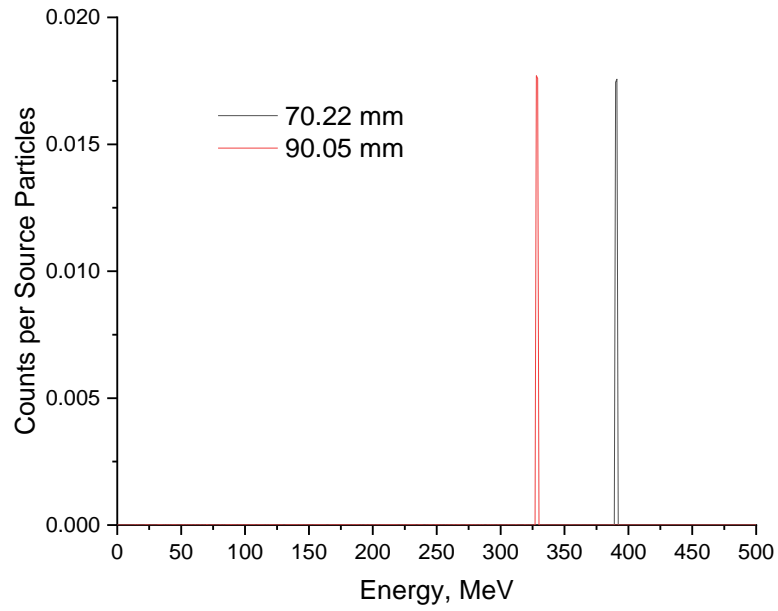


Figure 3. 3 Pulse Height Spectra of the MCNP/X simulation (top) and the experimental data (bottom) for 70.22mm and 90.05 mm BF

Figure 3.4 displays two peaks corresponding to 100.42 mm and 120.18 mm BF. MCNP/X data reveals that the beam imparts 290 MeV and 207 MeV. In contrast to the experimental data, the beam deposits 177 MeV and 141 MeV of energy, respectively.

Lastly, figure 3.5 exhibits two peaks for pulse height spectra for the BF at 130.33 mm and 143.16 mm. MCNP/X shows the deposited energy to be 150 MeV and 34 MeV, respectively. However, the experimental result, indicates that the energy deposited is 112 MeV and 40 MeV, respectively.

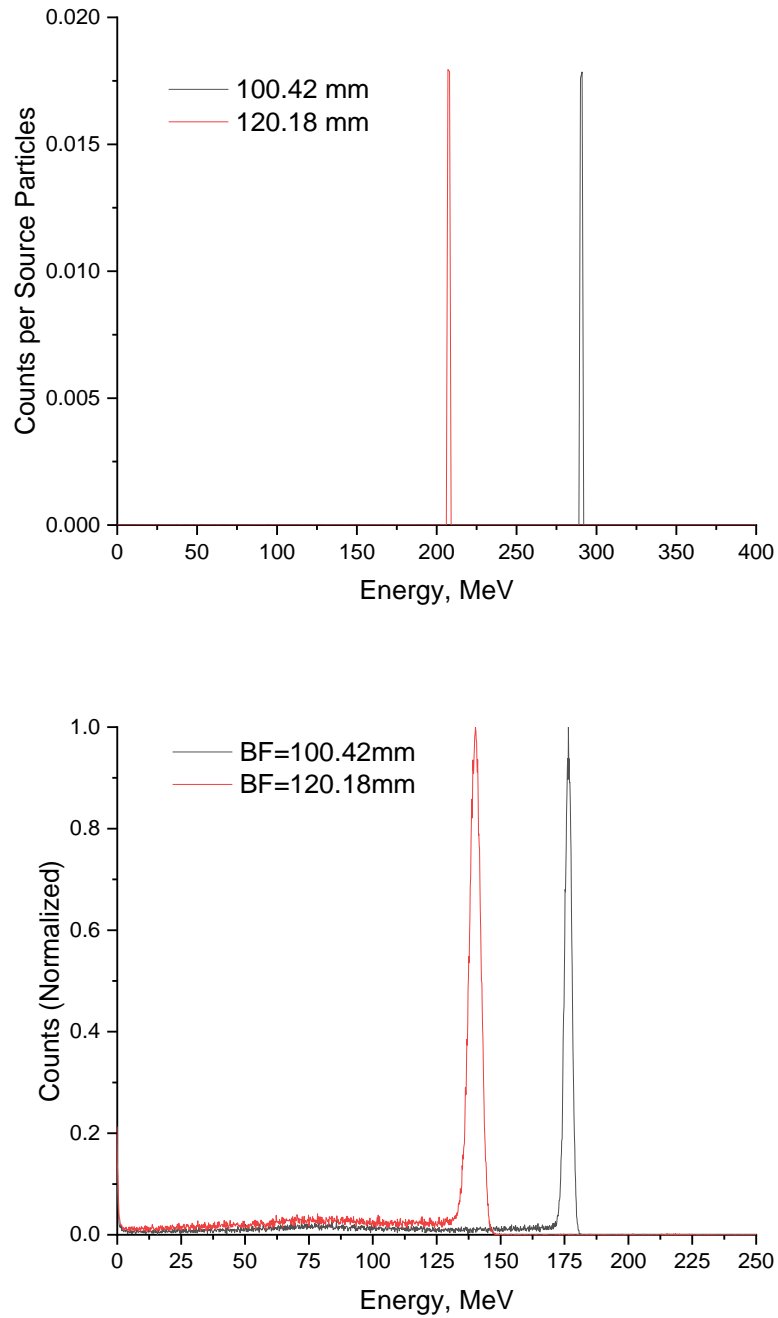


Figure 3. 4 Pulse Height Spectra of the MCNP/X simulation (top) and the experimental data (bottom) for 100.42mm and 120.18 mm BF

Overall, comparing the energy the He ion deposits in the LaBr_3 crystal between the MCNP/X simulations and the experimental results, reveals that the LaBr_3 detector measures the peak energy values of the He ion beam much lower than what is expected. MCNP/X code indicates the theoretical peak energy values that should be measured in the spectra. The MCNP/X peak energies represent the energy the He ion beam should exit out of the given BF. In all BF thicknesses presented in figures 3.1-3.5, the experimental spectra measure lower than the MCNP/X spectra.

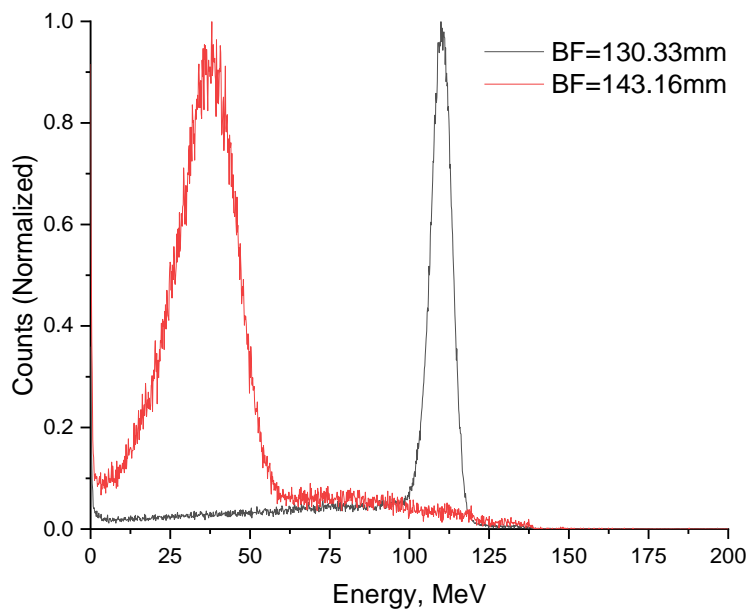
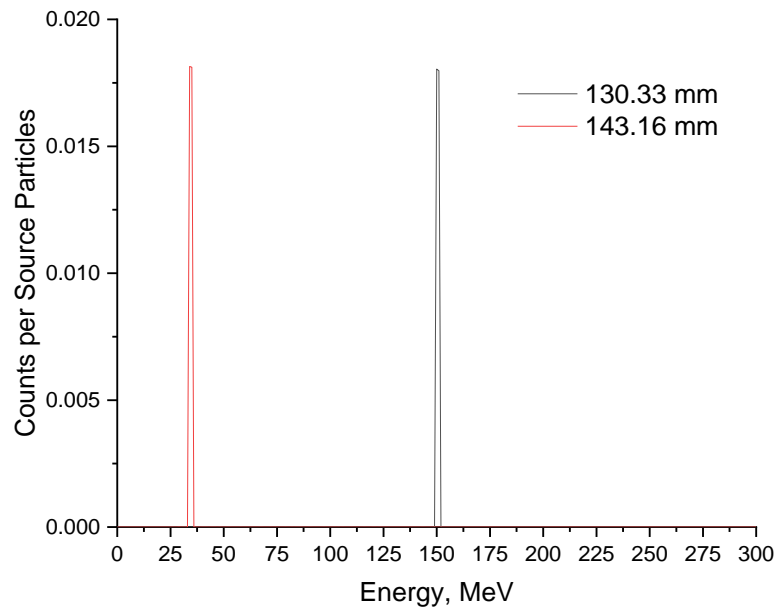


Figure 3. 5 Pulse Height Spectra of the MCNP/X simulation (top) and the experimental data (bottom) for 130.16 mm and 143.16 mm BF

3.4 Deposited Energy Curve

Figure 3.6 presents the deposited energy into the scintillator crystal of the He ion with respect to the binary filter thickness from the MCNP/X and experimental data. For both sets of data, the energy that is deposited increases with increasing thickness from the BF up until 40 mm. In this range, the energy of the He ion beam is too high for the full energy to be deposited in the scintillator crystal. Therefore, the beam passes through the crystal leaving only a fraction of the energy inside the active volume.

After 40 mm, the deposited energy decreases as the BF increases until the very end where the energy falls off much more with higher thickness; around 120 mm. The stopping power is not linear, as the energy of the beam decreases, the increase in stopping power becomes much greater. This is presented in the Bragg peak that is mentioned in the previous chapter, where most of the energy lost for a heavy charged particle is at the end of its path length. This is because, as the particle loses energy, it interacts more with the surrounding electrons in the medium and thus loses energy at a greater rate.

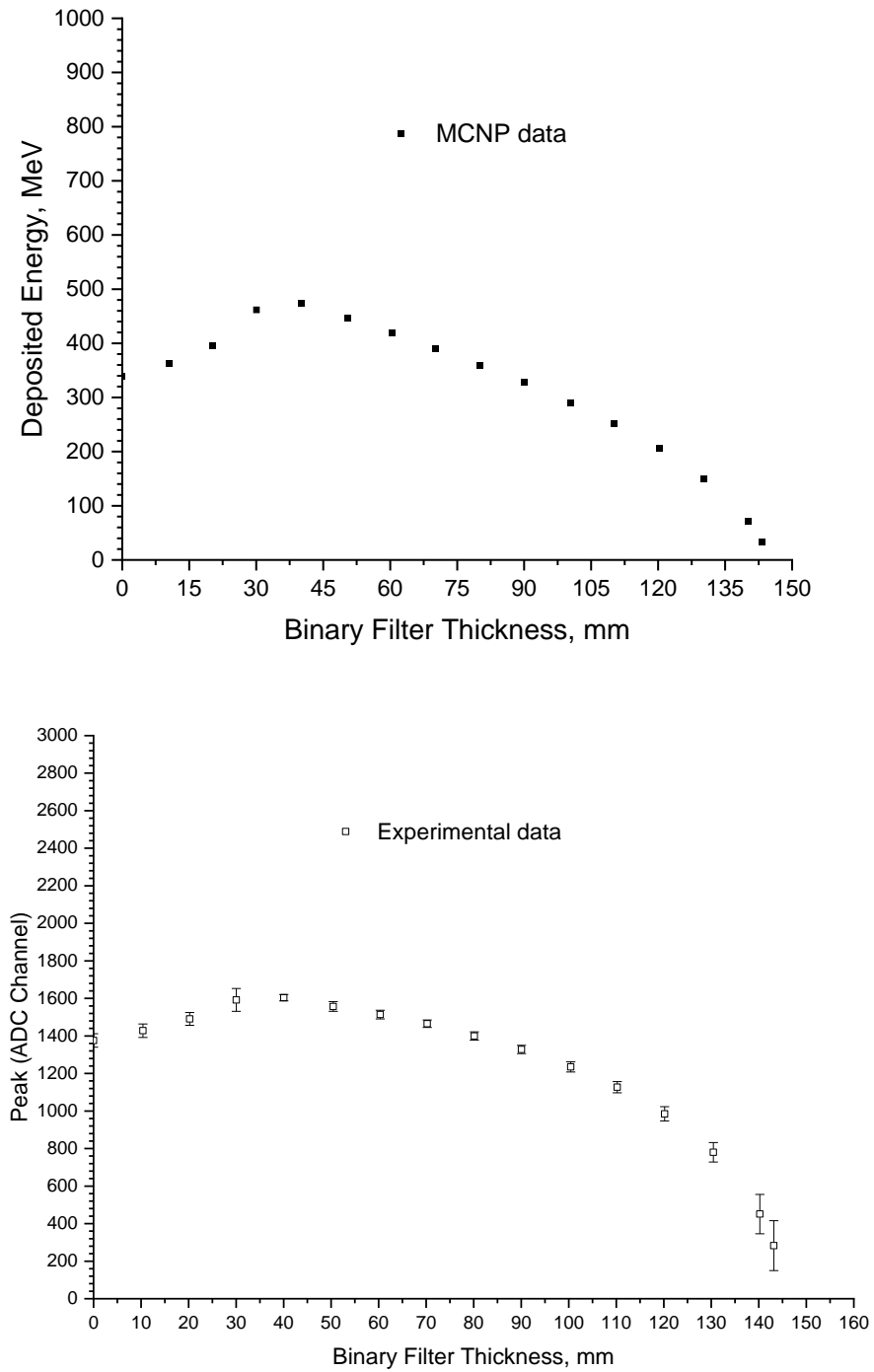


Figure 3. 6 The peak energies in the crystal with respect to BF thickness for the MCNP/X data (top) and the peak channel for the experimental data (bottom)

3.5 Response function

The response curve is produced using the peak energy values at various BF thicknesses for both the MCNP/X simulation and experimental peak data. Using both sets of data the response curve of the LaBr_3 crystal was produced. Figure 3.5 displays the experimental peak energy with respect to the simulation peak energies. The gamma calibration line is also shown to compare the crystal response to the He ion beam to the gamma ray response.

Figure 3.6 outlines the full response curve that includes the gamma source peak that was used to calibrate the detector. The abscissa in the response function in figure 3.6 represents the energy equivalent of the gamma deposited energy, $MeeV$. The full response curve summarises the gamma energy equivalent $MeeV$ as a function of the true energy. The LaBr_3 crystal response curve in figure 3.6 reveals that for the high-energy He ions, the scintillator becomes saturated and does not output light linearly with the energy deposited into the crystal from the He ion beam.

As discussed in chapter 1, the light output of the detector is defined as the number of photons created per unit of energy that is imparted into the scintillator material. The light output should ideally be linear. Examining the gamma calibration line indicates that an increase of energy in the crystal is a linear increase in the light output. Comparing the gamma response with He ions, one can see that the light output decreases below the gamma line after certain energy. It also decreases further as the deposited energy increases. The curve indicated a clear divergence starting at 70 MeV onwards.

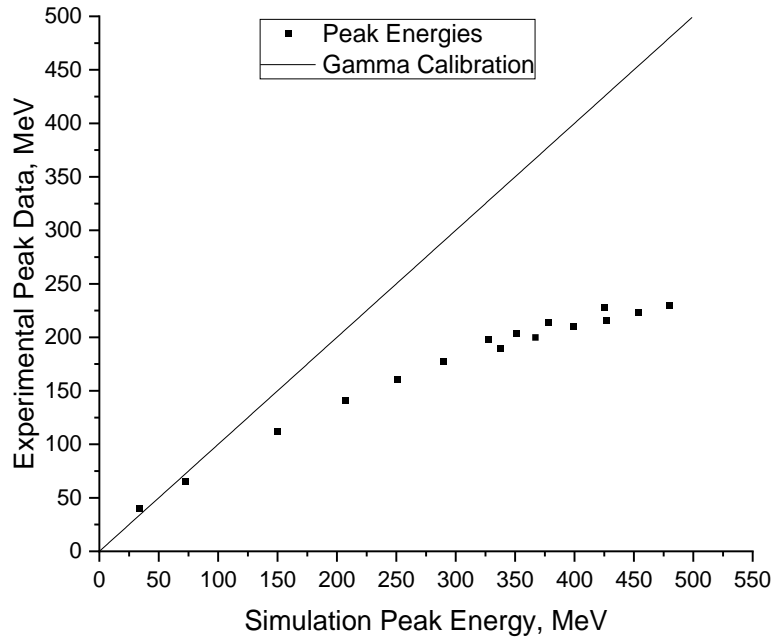


Figure 3. 7. The experimental peak energy with respect to the simulation peak energy along with the gamma calibration.

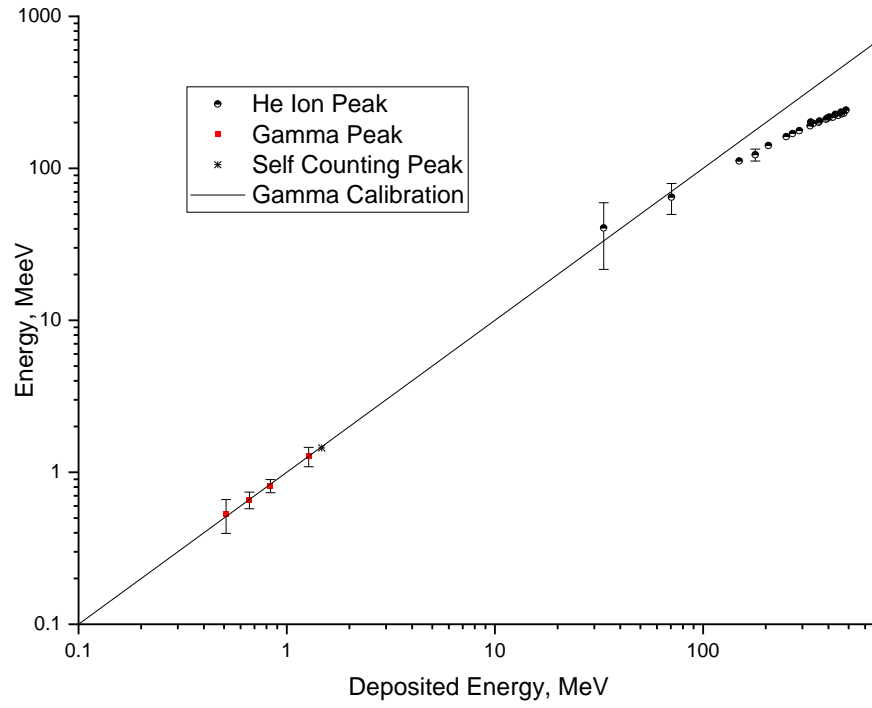


Figure 3. 8. Full response curve of the crystal with the gamma peak and calibration with the He ion peak energies.

3.6. Quenching effecting in He Ions

For gamma radiation, the light output is linear to the energy deposited. From the response curve this is not the case for He ions, there seems to be a point where the light output from the experimental peak energies is not proportional to the deposited energy compared to the simulation data.

When the crystal is exposed to gamma rays, there is a large amount of light produced from the photoelectrons via the excitations along the path of the gamma rays [20]. However, helium is a heavy particle. Due to the mass and charge of the particle, the He ion excites and ionizes a substantial portion of the crystal. Furthermore, a large amount of small energy, short-range delta rays are created along the path. When the He ions continue to bombard the crystal, a sizable portion of the crystal has already been excited or ionized. There is no increase of light output from the crystal since the number of excited states reaches its limit; a point of saturation in the number of excitations in the crystal to produce light. In addition to this, delta rays could overlap with one another thus further decreasing the amount of light that could be produced inside the crystal [5,32,37].

This quenching effect has been observed in organic plastic scintillators and Bismuth Germanate (BGO) crystal response investigated at the HIMAC facility using several heavy ions as well [32,37]. Like it is shown in the response curve in Figure 3.6, the light output from the heavy-ion shows the quenching effect.

3.7 Detector Characteristics

3.7.1 Detector Resolution

The detector resolution at various thicknesses of the BF is calculated. The FWHM is outlined for various thicknesses in Figures 3.7-3.9. Figure 3.7 presents BF thickness of 10.41 mm for absorption peak at 360 MeV, the resolution was determined to be 1.9%

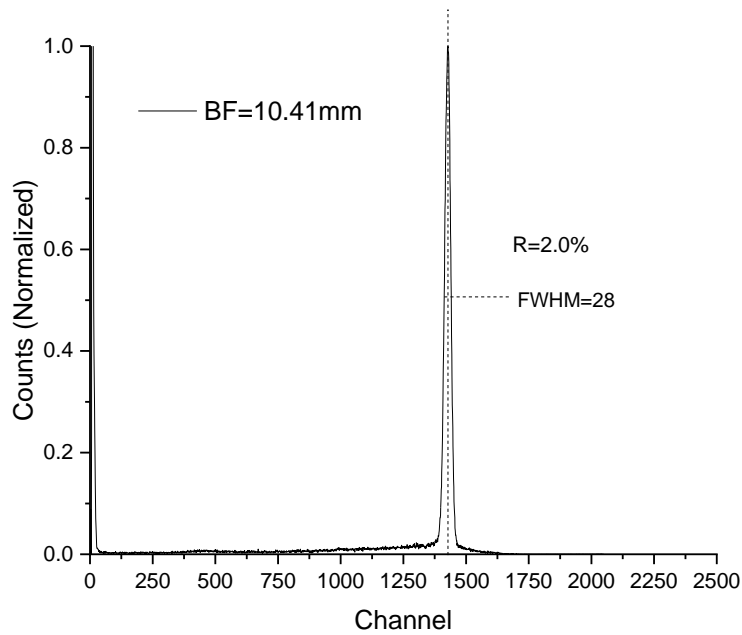


Figure 3. 9 FWHM of the full peak at 10.41 mm BF

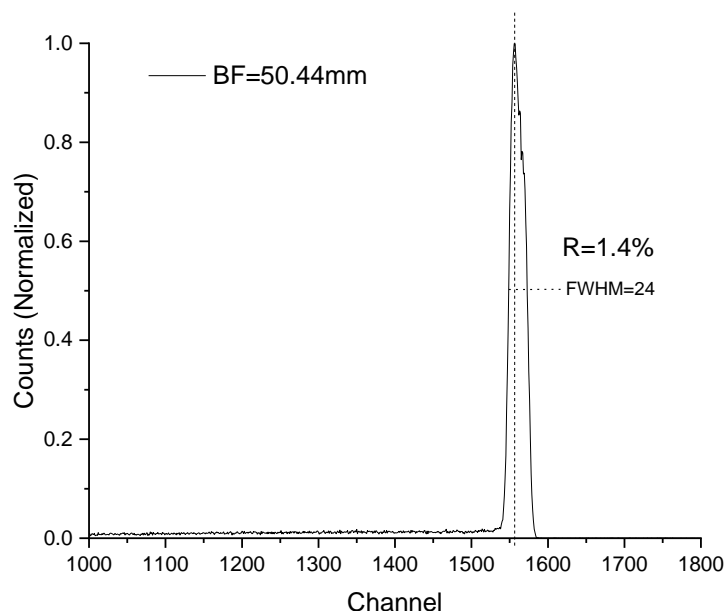


Figure 3. 10 FWHM of the full peak at 50.41 mm BF

Figure 3.8 shows the peak of 50.22 mm, the deposited energy is 450 MeV with an FWHM value of 21.82, and the resolution was determined to be 1.4%. Figure 3.9 displays the spectra at 140.22 mm, depositing 72 MeV energy. The FWHM is determined to be 116, the resolution was calculated to be 26%. The resolution does not change significantly between 10.41 mm and 50.44 mm. However, the detector resolution is worse jumping to 24% at 140.22 mm. Furthermore, the resolution at 143.16 mm gets worse at 53%. This could be caused by wider energy ranges of the He ion exiting out of the BF at larger thicknesses due to the increased ion straggling occurring in the BF.

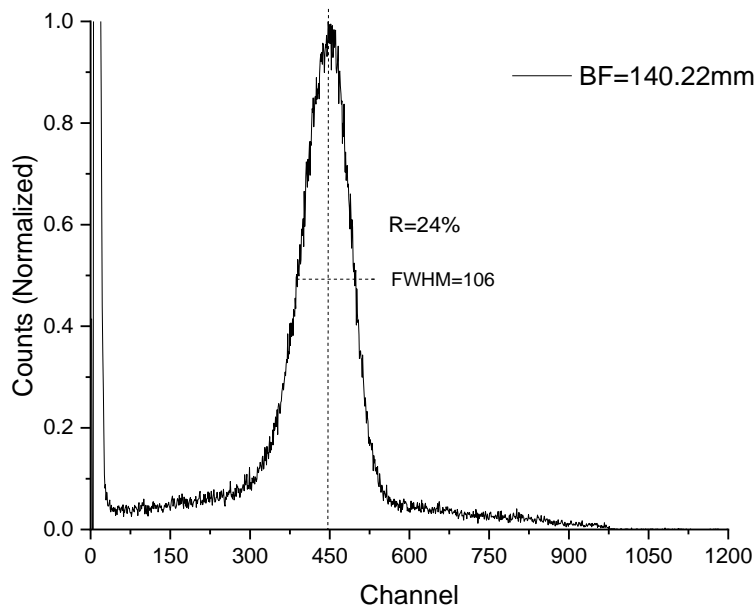


Figure 3. 11 FWHM of the full peak at 140.22 mm BF

3.7.2 Error Analysis

The error presented in Figures 3.6 and 3.9 for the experimental measurements, sigma is defined as half the FWHM for the absorption peak for measurements at a 95% confidence level. The FWHM are defined for the specific peak in figures 3.9-3.11 and an example of the calculation is presented in Appendix D. Notable peaks with unusually high errors and resolutions are the measured peaks at 140.22 mm and 143.16 mm with a FWHM of 104 and 150 channels, respectively. The high error could be due to the large fluctuation in energies of the ions leaving the BF. The BF is at a point where it is absorbing most of the ion energy. At this point, it could be statistical fluctuations of the interactions of the ions at the end of the BF.

Conclusions

In this study, a LaBr_3 scintillator crystal was exposed to high-energy He ions. This study was done at the HIMAC facility in Chiba, Japan. Using the dose depth curve, the He beam energy through the HIMAC was determined to be 145.35 MeV/n. To decrease the He ion beam energy, Binary Filters of varying thickness between the beam and the scintillator detector were used. This BF thickness ranged from 0 – 146.16 mm. Before the irradiation, the detector was calibrated using various gamma radiation sources. The pulse height spectrum from the scintillator was measured with each thickness of the binary filter.

Using the Monte Carlo code MCNP/X, the irradiation of the scintillator was simulated, and the response of the scintillator crystal was obtained. The pulse height spectrum was tallied from varying energies of He ions.

The pulse height spectra obtained from the experiment were compared to the spectra obtained using the MCNP/X code. Both spectra follow the trend, where the peak energies from 0 - 40 mm BF were increasing. After that range, the peak energies decreased as expected. Before 40 mm, the He ion beam energy is large enough that the particle passes the scintillator and only a portion of energy was deposited.

The response function was obtained by comparing the experimental and the simulated data from the modeling. Then comparing the peak position to the gamma calibration line. Comparing the peak to the gamma calibration shows that there is a quenching effect on the scintillator crystal. This decreases the light output of the scintillator crystal, thus having much lower peak energy measured than what should be theoretically on the spectra.

The resolution of the measured peaks ranged from 1.4% - 53%. These large errors are associated with the last two BF thickness at 140.22 mm and 143.16 with an FWHM at a resolution of 26% and 53%. This could be due to large fluctuations in the energy exiting the BF, as is it approaching the full range of the He Ions.

Future Work

Future work would be to further the characterization of LaBr_3 detectors to other heavy ions to fully understand how these detectors respond in the presence of heavier ions. Further investigating how the quenching effects observed in this thesis change with heavier ions. The goal being able to identify these quenching effects during the measurement of future space missions.

References

- [1] F. N. Flakus, Detecting and measuring ionizing radiation - a short history, IAEA Bulletin, Vol 23, No 4, 1981.
- [2] G. F. Knoll, Radiation Detection and Measurement, John Wiley & Sons, 3rded, 2000.
- [3] N. J. Cherepy, B. W. Sturm, O. B. Drury, T. A. Hurst, S. A. Sheets, L. E. Ahle, C. K. Saw, M. A. Pearson, S. A. Payne, A. Burger, L. A. Boatner, J. O. Ramey, E. V. van Loef, J. Glodo, R. Hawrami, W. M. Higgins, K. S. Shah, and W. W. Moses, SrI₂ Scintillator for Gamma Ray Spectroscopy, Proc. SPIE, 7449, 7449-0, 2009.
- [4] Cember, H., & Johnson, T. *Introduction to Health Physics*. McGraw Hill Medical. 2009
- [5] Tajudin, S. M., Namito, Y., Sanami, T., & Hirayama, H. Response of plastic scintillator to gamma sources. *Applied Radiation and Isotopes*, 159(Complete), 2020
- [6] Saint Gobain, BrillLanCe™ Scintillators Performance Summary, 2009.
- [7] S. N. Ahmed, Physics and Engineering of Radiation Detection, Academic Press Inc. Published by Elsevier, 1sted, 2007.
- [8] J. R. Lamarch, Introduction to Nuclear engineering, Prentice-Hall, Inc., 3rd ed, 2001.
- [9] Owens, A. Scintillators on Interplanetary Space Missions. *IEEE Transactions on Nuclear Science*, 55(3, 2), 1430–1436, 2008
- [10] Oberstedt, A., Billnert, R., & Oberstedt, S. Gamma-ray Measurements with LaBr₃: Ce Detectors -thinking Outside the Box. *Physics Procedia*, 31, 21–28, 2012
- [11] Camera, F., Blasi, N., Brambilla, S., Crespi, F. C. L., Idini, A., Maiolino, C., Nicolini, R., Riboldi, S., Santonocito, D., Sassi, M., & Wieland, O. (2007). Investigation of the self activity and high energy γ -rays response of a 1" \times 1" and 3" \times 3" LaBr₃:Ce scintillators. *2007 IEEE Nuclear Science Symposium Conference Record*, 2, 1386–1388.
- [12] Abbas, M. I., & Noureddeen, S. (2011). Analytical expression to calculate total and full-energy peak efficiencies for cylindrical phoswich and lanthanum bromide scintillation detectors. *Radiation Measurements*, 46(4), 440–445.
- [13] Miller, A., Machrafi, R., & Mohany, A. Development of a semi-autonomous directional and spectroscopic radiation detection mobile platform. *Radiation Measurements*, 72(Complete), 53–59. <https://doi.org/10.1016/j.radmeas.2014.11.009>, 2015
- [14] Young-Yong Ji, Hee-Yeoul Choi, Wannoo Lee, Chang-Jong Kim, Hyun-Sock Chang, & Kun-Ho Chung. Application of a LaBr₃(Ce) Scintillation Detector to an Environmental Radiation Monitor. *IEEE Transactions on Nuclear Science*, 65(8_Part_2), 2021–2028. <https://doi.org/10.1109/TNS.2018.2823322>, 2018
- [15] J. F. Briesmeisr, MCNP-A General Monte Carlo N-Particle Transport Code, Vol 4B, 1997.

- [16] X-5 Monte Carlo Team, MCNP-A General Monte Carlo N-Particle Transport Code, Vol 1, 5th Ed, 2003, Rev (2008).
- [17] J. K. Shultis and R. E. Faw, AN MCNP PRIMER, Rev 2005.
- [18] A. L. Schwarz, R. A. Schwarz, and L.L. Carter, MCNP/MCNPX Visual Editor Computer Code Manual, 2008.
- [19] J. F. Ziegler, M. D. Ziegler, and J. P. Biersack, —SRIM – The stopping and range of ions in matter (2010), | Nucl. Instrum. Methods Phys. Res. Sect. B Beam Interact. Mater. At., vol. 268, no. 11–12, pp. 1818–1823, 2010.
- [20] M. Moszyński, M. Balcerzyk, W. Czarnacki, M. Kapusta, W. Klamra, P. Schotanus, A. Syntfeld, M. Szawlowski, and V. Kozlov, “Energy resolution and non-proportionality of the light yield of pure CsI at liquid nitrogen temperatures”, Nucl. Instr. and Meth. A 537, pp. 50, 2005.
- [21] P. Dorenbos, J.T.M. de Haas, C.W.E. van Eijk, IEEE Trans. Nucl. Sci. NS-51 (3), 2004.
- [22] E. V. D van Loef, P. Dorenbos, C.W.E van Eijk, K.W Krämer, and H.U Güdel, “Scintillation properties of LaBr₃: Ce³⁺ crystal: Fast efficient and high-energy-resolution scintillators”, Nucl. Instr. and Meth., A 486, pp. 254, 2002.
- [23] G. Anil Kumar, I. Mazumdar, and D. A. Gothe, “Efficiency calibration and simulation of a LaBr₃(Ce) detector in close-geometry”, Nucl. Instrum. Meth., A. 609, pp.183, 2009.
- [24] M. Moszyński, A. Nassalski, A. Syntfeld-Każuch, T. Szcześniak, W. Czarnacki, D. Wolski, G. Pausch, and J. Stein, “Temperature dependences of LaBr₃(Ce), LaCl₃(Ce) and NaI(Tl) scintillators”, Nucl. Instrum. Meth., A. 568, no. 1–2, pp.739, 2006.
- [25] F.G.A. Quarati, Alan Owens, P. Dorenbos, J.T.M. de Haas, G. Benzoni, N. Blasi, C.Boiano, S. Brambilla, F. Camera, R. Alba, G. Bellia, C. Maiolino, D. Santonocito, M. Ahmed, N. Brown, S. Stave, H.R. Weller, and Y.K. Wu, “High energy gamma-ray pectroscopy with LaBr₃ scintillation detectors”, Nucl. Instrum. Meth., vol. 629, no. 1, pp.157, 2011.
- [26] F. Quarati, A.J.J. Bos, S. Brandenburg, C. Dathy, P. Dorenbos, S. Kraft, R.W. Ostendorf, V. Ouspenski, and A. Owens, “X-ray and gamma-ray response of a 2”×2” LaBr₃: Ce scintillation detector” , Nucl. Instr. and Meth. A 574, pp 115, 2007.
- [27] M. Ciemała, D. Balabanski, M. Csatlós, J.M. Daugas, G. Georgiev, J. Gulyás, M. Kmiecik, A. Krasznahorkay, S. Lalkovski, A. Lefebvre-Schuhl, R. Lozeva, and A. Maj, A. Vitez, “Measurements of high-energy g-rays with LaBr₃: Ce detectors”, Nucl. Instr. and Meth. A 608, pp 76, 2009.
- [28] B.D. Milbrath, B.J. Choate, J.E. Fast, W.K. Hensley, R.T. Kouzes, and J.E. Schweppe “Comparison of LaBr₃: Ce and NaI(Tl) scintillators for radio-isotope identification devices”, Nucl. Instr. and Meth, A 572 pp. 774, 2007.

- [29] A. Favalli, H.-C. Mehner, and F. Simonelli , “Wide energy range efficiency calibration for a lanthanum bromide scintillation detector”, *Radiat. Meas.* 43, pp.506, 2008.
- [30] M. Moszynski, Ł.S. Widerski, T. Szczeniowski, A. Nassalski, A. Syntfeld-Kazuch, W. Czarnacki, G. Pausch, J. Stein, P. Lavoute, F. Lherbert, and F. Kniest, “Study of LaBr₃ Crystals Coupled to Photomultipliers and Avalanche Photodiodes”, *Nuclear Science Symposium Conference Record, NSS '07. IEEE*, 2007.
- [31] R. Pani, R. Pellegrini, M.N. Cinti, P. Bennati, M. Betti, F. Vittorini, M. Mattioli, G. Trotta, V. Orsolini Cencelli, R. Scafe, L. Montani, F. Navarra , D. Bollini, G. Baldazzi, G. Moschini, P. Rossi, F. de Notaristefani, “LaBr₃:Ce crystal: The latest advance for scintillation cameras”. *Nucl. Instr. and Meth. A* 572, pp.268, 2007.
- [32] Becchetti, F. D., Thorn, C. E., & Levine, M. J. (1976). Response of plastic scintillator detectors to heavy ions, *Z* 35, E 170 MeV. *Nuclear Instruments and Methods*, 138(1), 93–104.
- [33] HAMAMATSU PHOTONICS. Photomultiplier tubes basics and application (3rd ed.). 2017
- [34] Source to detection, for the educator and professional. *Spectrum Techniques*. (n.d.). Retrieved February 16, 2022, from <https://www.spectrumtechniques.com/>, 2020
- [35] Osprey Universal Digital MCA tube base for scintillation spectrometry. *Universal Digital MCA Tube Base for Scintillation Spectrometry*. (n.d.). Retrieved 2022, from <https://www.mirion.com/products/osprey-universal-digital-mca-tube-base-for-scintillation-spectrometry>, 2017
- [36] Uchihori, Y. (n.d.). HIMAC Facility. https://www.nirs.qst.go.jp/ENG/rd/1ban/himac_inf.html , 2006
- [37] Matsufuji, N., Kanai, T., Komami, H., & Kohno, T. (1999). The response of a BGO scintillator to relativistic heavy ions. *Nuclear Instruments and Methods in Physics Research Section A: Accelerators, Spectrometers, Detectors and Associated Equipment*, 430(1), 60–68.
- [38] Janis. Nuclear Energy Agency (NEA). (n.d.), from https://www.oecd-nea.org/jcms/pl_39910/janis , 2020

Appendix

Appendix A

MCNP/X Simulation Code

c Detector Response Function with Heavy Charge

c particle sources

c

c -----

c cell cards

1 1 -5.08 -1

2 0 1 -2

3 0 2

c -----

c surface cards

1 rcc 0 -1 0 0 2 0 0.8

2 sph 0 0 0 100

c -----

c mode

mode a

c -----

c material card

m1 57000. 1 \$MAT1

35000. 3

imp:a 1 1r 0 \$ 1, 3

phys:a 600

c -----

c source card

c Source Cards

sdef pos=0 -11 0 axs=0 1 0 erg=34 par=A &

vec=0 1 0 dir=1 rad=d1

si1 0 10

sp1 -21 1

c -----

c Tally cards

c

f8:a 1

ft8 GEB 0 0.02 0

e8 0 599I 600

c

c -----

c execution control

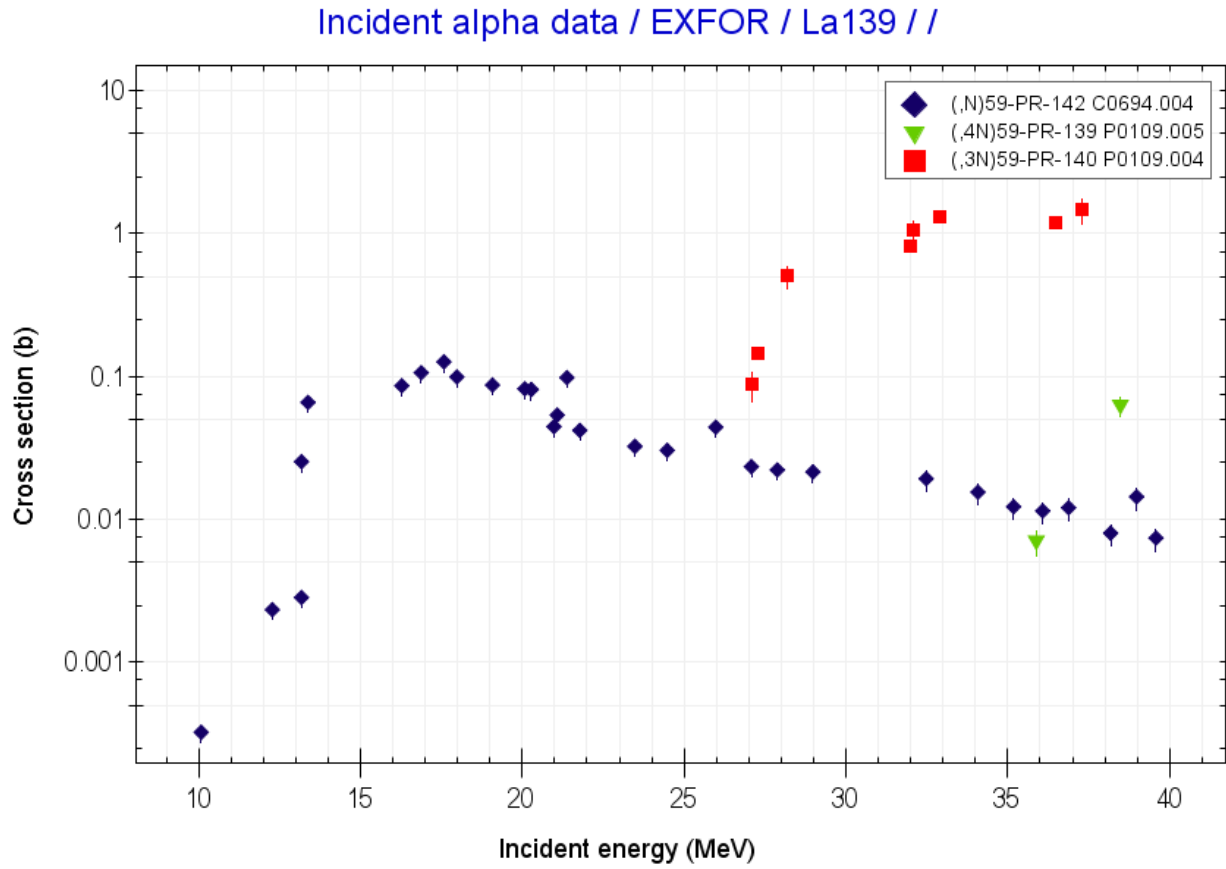
c

nps 1000000

c -----

Appendix B

Cross-Sectional Data of Alpha particles with La-137 and Br-79 [38]

**Figure B. 1 Cross-Sectional Data for La-137**

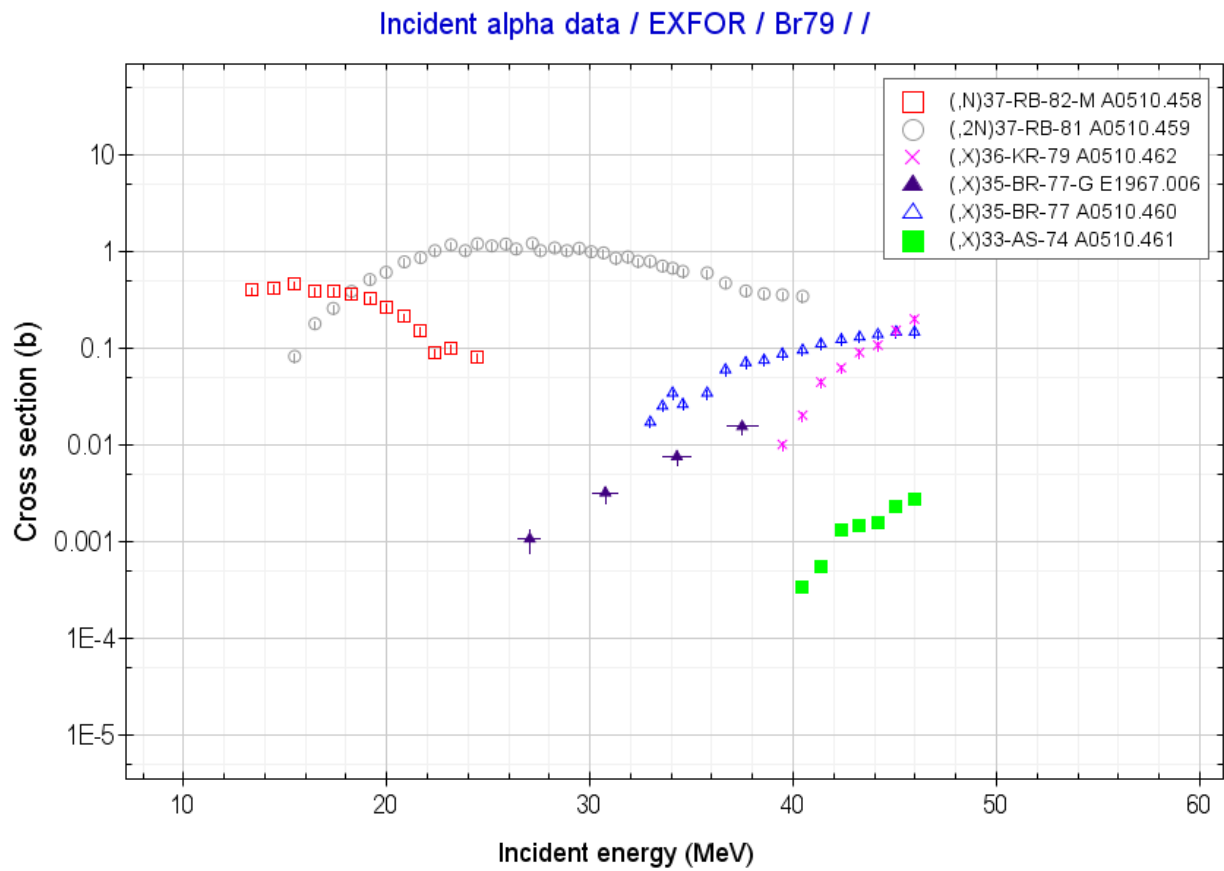


Figure B. 2 Cross-Sectional Data for Ba-49

Appendix C

Example Calculation of the Beam Energy coming out of the BF using the SRIM Table

For BF at 60.32 mm:

Max range of He ion in BF (water) = 147.87 mm

$147.87 \text{ mm} - 60.32 \text{ mm} = 87.55 \text{ mm}$

According to the SRIM table, the He ion energy at 94.14 mm is 450 MeV

Stopping power at 450 MeV according to SRIM = 2.693 keV/micron

$95.14 \text{ mm} - 87.55 \text{ mm} = 7.62 \text{ mm} = 7620 \text{ microns}$

Energy lost between 95.14 mm - 87.55 mm = $2.693 \text{ keV/micron} * 7620 \text{ microns} = 20520 \text{ keV}$

Energy of the He ions coming out the BF = $450000 \text{ keV} - 20520 = 429479 \text{ keV} = 429.48 \text{ MeV}$

| Ion Energy | dE/dx Elec. | dE/dx Nuclear | Projected Range | Longitudinal Stragglng | Lateral Stragglng |
|------------|-------------|---------------|-----------------|------------------------|-------------------|
| 400.00 MeV | 2.938E+00 | 1.336E-03 | 76.36 mm | 2.90 mm | 963.00 um |
| 450.00 MeV | 2.693E+00 | 1.198E-03 | 94.14 mm | 3.85 mm | 1.18 mm |
| 500.00 MeV | 2.495E+00 | 1.087E-03 | 113.42 mm | 4.73 mm | 1.41 mm |
| 550.00 MeV | 2.331E+00 | 9.956E-04 | 134.15 mm | 5.57 mm | 1.66 mm |
| 581.40 MeV | 2.244E+00 | 9.458E-04 | 147.87 mm | 5.91 mm | 1.82 mm |



60.32 mm

Figure C. 1 SRIM output table used for beam energy calculation for 60.32 mm BF

Appendix D

Example calculation for peak FWHM and resolution

For BF at 140.22 mm

Peak channel (H_0): 447

Channels at half maxima (n_1, n_2): 392, 498

FWHM = $n_2 - n_1 = 498 - 392 = 106$ channels

Resolution: $\text{FWHM}/H_0 = 106/447 = 0.24 = 24\%$

Error:

$\sigma = \text{FWHM}/2 = 53$ channels

At 95% confidence, the error = $1.96 * \sigma = \pm 104$ channels

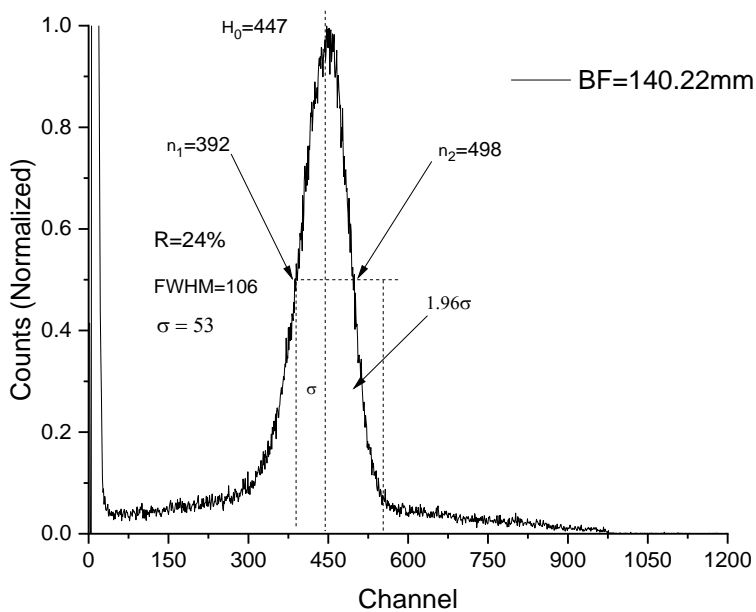


Figure D. 1 Resolution and error analysis for 140.22 mm BF

Appendix E

Contribution to Knowledge

[1] Christian Nayve, Rachid Machrafi, Alex Miller, Eyad Tamimi, Zhe Li “Study of the LaBr₃ Scintillator Response to Helium Ions”, CNSC, June 2021.

[2] Zhe Li, Rachid Machrafi, Eyad Tamimi, Christian Nayve, “Development of Neutron Monitor for Fusion Systems”, CNSC, June 2021.

[3] Eyad Tamimi, Rachid Machrafi, Zhe Li, Christian Nayve “Evaluation of the Effectiveness of Light-Element Shielding Materials in Complex Radiation Fields”, CNSC, June 2021.